

Tabletop attosecond X-rays in the water window

Seunghwoi Han^{a,b}, Jie Li^{c,d}, Zheyuan Zhu^e, Andrew Chew^a,
Esben W. Larsen^f, Yi Wu^a, Shuo Sean Pang^e, Zenghu Chang^{a,*}

^aInstitute for the Frontier of Attosecond Science and Technology, CREOL and Department of Physics, University of Central Florida, Orlando, FL, United States

^bSchool of Mechanical Engineering, Chonnam National University, Gwangju, Republic of Korea

^cAcademy of Opto-Electronics, Chinese Academy of Sciences, Beijing, China

^dSchool of Optoelectronics, University of the Chinese Academy of Sciences, Beijing, China

^eCREOL, University of Central Florida, Orlando, FL, United States

^fQuantum Optics and Laser Science Group, Blackett Laboratory, Imperial College London, London, United Kingdom

*Corresponding author: e-mail address: zenghu.chang@ucf.edu

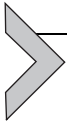
Contents

1. Introduction	2
2. Novel attosecond driving lasers	4
2.1 Optical parametric chirped pulse amplifiers at 1.6–2.1 μm	6
2.2 Cr:ZnSe chirped pulse amplifier centered at 2.5 μm	12
3. Isolated attosecond pulse generation in the water window	17
3.1 Phase-matched high harmonic generation in the water window	17
3.2 Sub-cycle gating techniques for isolated attosecond pulse	21
3.3 Atto-chirp compensation	24
4. Characterization of attosecond X-ray pulses	27
4.1 Attosecond streaking and FROG-derived attosecond pulse retrieval	27
4.2 Attosecond pulse retrieval with neural networks	33
4.3 Performance and comparisons of learning-based pulse retrieval methods	37
5. Applications in element-specific ultrafast spectroscopy	42
5.1 Attosecond X-ray transient absorption spectroscopy	44
5.2 Attosecond X-ray photoelectron spectroscopy	48
6. Summary and outlook	53
Acknowledgments	53
References	53

Abstract

In recent years, a new generation of attosecond driving lasers centered at $\sim 1.7 \mu\text{m}$ based on carrier-envelope phase stabilized Optical Parametric Amplification have enabled the generation of X-ray pulses reaching the water window (282–533 eV), which is of great interest given their applications in the study of electron dynamics in atoms, molecules and condensed matter containing carbon, nitrogen, oxygen and other

important elements. Various gating methods emanated isolated attosecond pulses for pump-probe experiments. Atto-chirp compensation has made the X-ray pulses at the carbon K-edge as short as 53 attoseconds. Novel spectral phase retrieval schemes such as neural network have been implemented to attosecond streaking techniques for faster and more reliable characterization of X-ray pulses. The water window X-ray sources have been applied to ultrafast measurements, such as attosecond transient absorption spectroscopy and photoelectron spectroscopy with element specificity and sub-optical-cycle temporal resolution.



1. Introduction

The generation of attosecond photon pulses for observing and controlling electron dynamics in atoms, molecules and condensed matter is the one of the most active frontiers in ultrafast science in the last two decades (Chang et al., 2016; Corkum and Chang, 2008; Krausz and Ivanov, 2009). Since the spectrum in the infrared and visible bands is not wide enough, coherent optical fields in ultraviolet and X-ray regime are needed to support attosecond pulses (Chang, 2011). Although attosecond X-ray pulses have been demonstrated with large-scale X-ray free electron lasers (Duris et al., 2020), it is difficult to develop tabletop attosecond lasers because of the lack of proper gain medium. High-order harmonic generation (HHG) is a coherent frequency conversion process arising from gaseous atoms or molecules when they are irradiated by an intense laser pulses that supports production of attosecond pulses. The HHG phenomenon was discovered in 1980s (Ferry et al., 1988; McPherson et al., 1987) and the temporal coherence of X-ray light was explained by a three-step semiclassical model (Corkum, 1993; Schafer et al., 1993). According to the model, an electron tunnels out from the Coulomb barrier of an atom in a strong laser field (step 1) is also accelerated by the same field (step 2). The returning electron wavepacket interfere with the remaining ground state standing wave, forming an oscillatory dipole that emits an attosecond pulse (step 3). This process periodically repeats itself every half cycle of the driving pulse, which naturally generates an attosecond pulse train (Paul, 2001). In 2001, the first isolated attosecond pulses was demonstrated by HHG (Hentschel et al., 2001), which is critical for pump-probe experiments. The development of high-power femtosecond near infrared (NIR) Ti:Sapphire laser with few-optical-cycle duration pioneered new area in strong-field physics and led to attosecond optical sources in the 15–150 eV photon energy range (Chini et al., 2014). There is a strong demand for

attosecond light sources in the water window, which is important for studying charge dynamics in molecules containing C, N and O that are relevant to photochemistry (Young et al., 2018).

The highest achievable photon energy from HHG predicted by the three-step model is determined by the maximum kinetic energy of the retuning electron. This cutoff photon energy $h\nu_{cutoff}$ based on single atom response is given by:

$$h\nu_{cutoff} = I_p + 3.17U_p \propto I_0\lambda_{IR}^2, \quad (1)$$

where I_p is the ionization potential of the target atom, U_p is the ponderomotive energy, I_0 is the laser intensity and λ_{IR} is the infrared (IR) driving laser wavelength. There are potentially two approaches to extend the cutoff to the water window for a given target element, i.e., increase the laser intensity or wavelength. However, the highest intensity that can be applied is limited by the depletion of the ground state (Chang et al., 1997).

The strong field approximation of high harmonic generation provides a quantum trajectory interpretation of the three-step semi-classical model (Lewenstein et al., 1994). There are two types of trajectories that contribute to X-ray emission, the so-called short and long, which correspond to the time between departure and return of the electron to the parent ion in one IR optical cycle. An isolated attosecond X-ray pulse measured experimentally may originate from a single short trajectory. An analytical expression of the complex dipole moment, the source of the isolated X-ray pulse, can be obtained by applying the saddle point approach (Nayak et al., 2019),

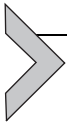
$$\begin{aligned} \tilde{D}(\omega_X) &\approx E_{IR}(t_i)a^*(t_i)d^*[p_s + A_{IR}(t_i)] \\ &\times \exp [i(\omega_X t_r - S(p_s, t_r, t_i) - I_p(t_r - t_i))] \left[\frac{\pi}{\varepsilon + i(t_r - t_i)/2} \right]^{3/2} \frac{2\pi i}{\sqrt{\text{del}[\Theta''_{\{t_i, t_r\}]}} \\ &\times a(t_r)d[p_s + A(t_r)], \end{aligned} \quad (2)$$

where $E_{IR}(t)$ and $A_{IR}(t)$ are the electric field and vector potential of the driving laser. t_i and t_r are the stationary values of the time that ionization (corresponding to first step of the semi-classical model) and recombination (third step) occur, respectively, that leads to the emission of the X-ray wave with frequency ω_X . $p_s = \int_{t_i}^{t_r} A_{IR}(t)dt/(t_r - t_i)$ is the canonical momentum. These complex quantities can be calculated from a set of saddle point equations. The spectral range of the X-ray is determined by the semi-classical

action $S(p_s, t_i, t_r) = \int_{t_i}^{t_r} \frac{1}{2} [p_s + A_{IR}(t)]^2 dt$. The total phase is $\Theta(p_s, t_i, t_r) = \omega_X t_r - S(p_s, t_i, t_s) - (t_r - t_s) I_p$. d is the complex dipole matrix element of the target atom, a is the complex amplitude of the ground state, which is related to the ionization probability of the atom, $p = 1 - aa^*$.

Obviously, the intensity of the HHG power spectrum $I_X(\omega_X) \propto \omega_X^4 |\tilde{D}(\omega_X)|^2$ diminishes when the ground state is completely depleted, i.e., $a \rightarrow 0$ or $p = 1$. Therefore there is an upper limit for the intensity that can be applied. In 1997, water window HHG was demonstrated with Ti:Sapphire lasers by driving the target atom close to this limit (Chang et al., 1997; Spielmann et al., 1997), but the X-ray intensity was too low for time-resolved experiments. In 2001, extending the HHG cutoff in the extreme ultraviolet region by using a long wavelength laser was first demonstrated (Shan and Chang, 2001), which paved the way for generating water window X-rays with high photon flux (Takahashi et al., 2008).

In this article, we review recent progress in the development of novel attosecond driving lasers in the short-wave infrared band (SWIR, 1.4–3 μm) based on few-cycle optical parametric chirped pulse amplification (OPCPA) and optical parametric amplifier (OPA), which enabled isolated attosecond pulse generation in the water window. We discuss the challenges in characterization of the X-ray pulses and introduce time-resolved spectroscopy applications where core to valence transitions provide element specificity.



2. Novel attosecond driving lasers

Most modern laser systems used for driving HHG mainly relies on frontend lasers based on titanium or ytterbium doped crystals as the gain medium. The most widely used laser for HHG is the titanium sapphire (Ti:Sapphire) lasers, which operate around 800 nm. The broad bandwidth of Ti:Sapphire allows for the generation of multi-millijoule laser pulses with sub-25 femtosecond (fs) durations (< 10 optical cycles) in as little as a single amplification stage (Lenzner et al., 1995). These specifications are ideal for driving HHG in the extreme ultraviolet (XUV, 15–150 eV), and for the past two decades these systems have been the main workhorse behind the development and expansion of attosecond (as) physics. These systems have been utilized for generating HHG (Papadogiannis et al., 2001); pulse compression down to the single-cycle limit and carrier envelope phase (CEP)

stabilization combined for generating single isolated attosecond pulses (Haworth et al., 2007; Mashiko et al., 2007); or used as a frontend pump for an optical parametric amplifier (DiChiara et al., 2012) or a chirped pulse optical parametric amplifier used for HHG (Yin et al., 2016). In the last few years ytterbium based frontends have slowly been gaining grounds on the Ti: Sapphire based systems within the field of attoscience. The surge of ytterbium-based frontends is driven by several favorable characteristics of the material and recent developments of the laser technology. For example, ytterbium doped yttrium aluminum garnet (Yb:YAG) has closely spaced absorption and lasing peaks in the near-infrared, which together with high-power near-infrared laser diodes allows for a high-average power high-efficiency lasers with minimal thermal load. This led to the first development of industrial grade picosecond (ps) and sub-ps ytterbium lasers centered at $1.03\ \mu\text{m}$ (Innerhofer et al., 2003). While the maximum pulse energy of ultrashort ytterbium lasers remains limited by their narrow bandwidth coupled with the accumulated B-integral within the laser chain, pulses with several hundreds of microjoule and durations above 150 fs with repetition rates of tens or hundreds of kHz have become readily accessible. The slightly longer picosecond lasers are mainly used as a pump source for next generation optical parametric chirped pulse amplifiers (Pupeikis et al., 2019), while the sub-ps lasers may be deployed in all the same ways for HHG as the Ti: Sapphire lasers described above (Beetar et al., 2019; Lorek et al., 2014).

One of the main reasons OPAs and OPCPAs have been extensively deployed within the attosecond physics community in recent years is the possibility for shifting the driving laser wavelength toward the short-wave infrared (SWIR) and mid-wave infrared (MWIR, $3\text{--}8\ \mu\text{m}$) region. The HHG cutoff photon energy scales quadratic with wavelength at the same intensity (Shan and Chang, 2001). This means that if the laser systems can deliver the needed required focused intensities $\sim 10^{13}\text{--}10^{15}\ \text{W}/\text{cm}^2$ soft X-ray photons in the water window is generated by shifting to longer wavelengths (DiChiara et al., 2012). By utilizing few-cycle pulses higher peak intensities can more readily be achieved before the generation medium is saturated by the critical ionization for which HHG cannot be efficiently produced. Few-cycle SWIR pulses from both hollow-core fiber compressed pulses from an OPA (DiChiara et al., 2012) or directly from an OPCPA has been successfully deployed to generating harmonics covering the entire SXR water window ($>543\ \text{eV}$) (Johnson et al., 2018; Pupeikis et al., 2019).

2.1 Optical parametric chirped pulse amplifiers at 1.6–2.1 μm

The motivation of developing 1.6–2.1 μm optical parametric amplifier or optical parametric chirped pulse amplifier (Cerullo and De Silvestri, 2003) is the need for reliable HHG or attosecond light sources for explore ultrafast dynamics above 150 eV, which is rarely fulfilled with near infrared drivers. The main advantage of parametric amplification over rare earth gain medium is the possibility to phase match and amplify a broad spectral range. By operating near the degeneracy condition, where the signal/idler wavelength is close, the gain bandwidth is close to one octave span (Cerullo and De Silvestri, 2003). Therefore, a high energy pulse with two or three cycles can be generated directly from amplifiers with proper dispersion compensation. The parametric wave mixing process can offer an optical gain larger than few hundreds for a single pass. Therefore, to increase the pulse energy from few nJ to mJ level, only two to three OPA/OPCPA stages are required. The typical pump to signal conversion efficiency is 10–30% in the final booster stage of the broadband OPA/OPCPA. Other advantage such as passive carrier-envelope phase stability caused by different frequency generation (DFG) between two phase locked pulses (Baltuška et al., 2002) is attractive for isolated attosecond pulse generation.

In a OPA/OPCPA, the parametric gain is determined by the instantaneous pump intensity and the phase match efficiency (Boyd, 2008). For femtosecond OPA, a thin crystal and high pump intensity combination is favored to reach broad bandwidth with sufficient gain. In an OPCPA, the gain spectrum can also be reshaped by tailoring the temporal profile of the pump pulse, which is not applicable in OPA or rare earth gain medium. Additional advantages of an OPCPA includes the tolerance to pump-seed delay jitter since they are both picosecond pulses.

2.1.1 Nonlinear crystal for broadband OPA/OPCPA at SWIR and MWIR range

A suitable nonlinear crystal for parametric amplification should have a relative large nonlinear coefficient for effective energy transfer from pump to signal wave (Dmitriev et al., 1999), a broad phase matched gain bandwidth for supporting few-cycle pulse and a low loss at the wavelength of interest. The amplification of signal field intensity can be analytically calculated (Cerullo and De Silvestri, 2003) using Eq. (3) by assuming an undepleted pump wave.

$$I_s(L) = I_{s0} \left[1 + \frac{r^2}{g^2} \sinh^2(g\Gamma) \right], \quad (3)$$

where

$$g = \sqrt{\Gamma^2 - \left(\frac{\Delta k}{2}\right)^2}, \quad (4)$$

$$\Gamma^2 = \frac{8\pi^2 d_{\text{eff}}^2 I_p}{\lambda_p \lambda_i \epsilon_0 c_0 n_s n_i n_p}, \quad (5)$$

where the I_{s0} and $I_s(L)$ is the signal field intensity at the front and exit face of crystal with length L , d_{eff} is the effective nonlinear coefficient, and $\Delta k = k_p - k_s - k_i$ is the wave vector mismatch. The subscripts p , s and i indicate the pump, signal and idler field, respectively. The wave vector mismatch is usually approximated using a Taylor expansion in terms of frequency.

$$\begin{aligned} \Delta k = \Delta k_0 + \left(\frac{\partial k_s}{\partial \omega_s} - \frac{\partial k_i}{\partial \omega_i} \right) \Delta \omega + \frac{1}{2!} \left(\frac{\partial^2 k_s}{\partial^2 \omega_s} - \frac{\partial^2 k_i}{\partial^2 \omega_i} \right) (\Delta \omega)^2 \\ + \frac{1}{3!} \left(\frac{\partial^3 k_s}{\partial^3 \omega_s} - \frac{\partial^3 k_i}{\partial^3 \omega_i} \right) (\Delta \omega)^3 \dots \end{aligned} \quad (6)$$

$\Delta k_0 = 0$ for perfect phase matching, $\Delta \omega = \Delta \omega_s = \omega_s - \omega_0$ denotes the offset from a central angular frequency ω_0 for the signal wave, the idler frequency change $\Delta \omega_i$ equals $-\Delta \omega_s$ by energy conservation. In degeneracy condition, the odd terms in the Taylor expansion vanishes since $k_s = k_i$, thus leaving only the second order $\partial^2 k_s / \partial^2 \omega_s + \partial^2 k_i / \partial^2 \omega_i$ and high order terms, which corresponds to the group velocity dispersion of signal and idler pulse. One can choose to operate the OPA/OPCPA at zero dispersion point $\partial^2 k_s / \partial^2 \omega_s = 0$, so the wave vector mismatch only includes the fourth and higher order terms.

Table 1 shows several crystals that can support ultra-broadband OPA schemes in degeneracy condition (Petrov et al., 2010). Only pump wavelength below $1 \mu\text{m}$ is listed. With commonly available pump source from the Ti:Sapphire ($\approx 0.8 \mu\text{m}$) or Yb:YAG ($\approx 1.0 \mu\text{m}$) laser. The gain bandwidth could cover an octave spanning from 1.2 to $2.4 \mu\text{m}$ thus attracting much attention by the ultrafast community to develop few-cycle SWIR/MWIR systems for soft X-ray HHG/attosecond light source.

Table 1 Parameter of several crystals that can support ultra-broadband OPA schemes when pumped below $1\ \mu\text{m}$. λ_p is the pump wavelength for $\partial^2 k_s / \partial^2 \omega_s = 0$ at degeneracy case.

Crystal	λ_p [μm]	$\Delta\lambda$ [μm]	θ/φ [degree] or Λ [μm]	$1/\nu_p - 1/\nu_s$ [fs/mm]
KDP (ooe)	0.493	0.746–1.444	42.11	14
LBO (ooe/eoo) x–y/x–z	0.599	1.043–1.408	1.35	17.9
CLBO (ooe)	0.627	0.987–1.713	28.57	10.8
BBO (ooe)	0.716	1.203–1.767	21.33	15.2
BIBO (ooe) x–z	0.789	1.233–2.189	10.97	11.9
BIBO (eoo) x–z	0.81	1.237–2.345	35.11	31.5
PPSLT (eee)	0.825	1.486–1.856	21.56	189
PPKTP (eee)	0.895	1.471–2.286	32.54	141
LiNbO ₃ (ooe)	0.949	1.624–2.284	46.27	37.2
PPLN (eee)	0.957	1.647–2.272	27.93	161
KNbO ₃ (ooe) x–y	0.988	1.665–2.442	47.71	46.3
KNbO ₃ (ooe) y–z	1.004	1.681–2.497	15.63	17.8
LiIO ₃ (ooe)	1.04	1.784–2.488	20.13	16

$\Delta\lambda$ is the FWHM gain bandwidth for 5 mm long crystal and a pump intensity of $50\ \text{GW}/\text{cm}^2$. θ/φ and Λ is the phase matching angle and the period in birefringent and quasi-phase-matching, respectively, $1/\nu_p - 1/\nu_s$ is group velocity mismatch (GVM) parameter between pump and signal calculated for degeneracy operation.

Adapted from Petrov, V., Ghotbi, M., Kokabee, O., Esteban-Martin, A., Noack, F., Gaydardzhiev, A., Nikolov, I., Tzankov, P., Buchvarov, I., Miyata, K., Majchrowski, A., Kityk, I.V., Rotermund, F., Michalski, E., Ebrahim-Zadeh, M., 2010. Femtosecond nonlinear frequency conversion based on BiB₃O₆. *Laser Photon. Rev.* 4, 53–98. <https://doi.org/10.1002/lpor.200810075>.

2.1.2 Few-cycle short-wave infrared OPCPA laser system for attosecond science

In 2006, Fuji et al. demonstrated a $2.1\ \mu\text{m}$, CEP stabilized, three-cycle OPCPA based on the periodically poled lithium niobate (LiNbO₃) crystal (PPLN) pumped by a 5 mJ Nd:YLF laser at 1053 nm (Fuji et al., 2006). With an upgraded 20 mJ Yb:YAG disk pump laser, the signal pulse energy was increased to 1.2 mJ (Deng et al., 2012). In the same year, a two cycle, $1.6\ \mu\text{m}$ OPCPA system based on BiB₃O₆ (BIBO) crystal was demonstrated by Ishii et al. (2012), which is capable of generating attosecond supercontinuum in the water window by properly controlling the CEP.

The ideal wavelength for pumping BIBO perfectly matches the central wavelength of Ti:Sapphire laser at $0.8\ \mu\text{m}$. Therefore, BIBO becomes a suitable nonlinear crystal for updating attosecond driving laser from 0.8 to $1.6\ \mu\text{m}$. In 2016, Yin et al developed a $3\ \text{mJ}$, $1.7\ \mu\text{m}$ OPCPA system pumped by an $18\ \text{mJ}$, cryo-cooled multi-pass Ti:Sapphire laser (Yin et al., 2016). By utilizing the polarization gating technique, 53 attosecond pulses were demonstrated with a spectrum covering $100\text{--}330\ \text{eV}$ (Li et al., 2017).

To drive bright attosecond source at soft X-ray regime, these novel short-wave infrared OPCPA systems share similar design schemes (Fuji et al., 2006) to achieve CEP stable, few cycle at $\sim\text{kHz}$ repetition rate. As an example, the $1.7\ \mu\text{m}$ OPCPA system by Yin et al. is shown Fig. 1. The OPCPA system consists of two parts: a high power three stage Ti:Sapphire CPA laser serving mainly as the pump and an seed generation (signal) beam line covering $1.2\text{--}2.2\ \mu\text{m}$. The 14-pass amplifier can deliver $4\ \text{mJ}$ of uncompressed pulse, from which $2.6\ \text{mJ}$ is compressed down to $30\ \text{fs}$ by a pair of transmission grating. This femtosecond beam is spectrally broadened to $500\text{--}900\ \text{nm}$ by self-phase modulation (SPM) in a $350\text{-}\mu\text{m}$ -diameter, 1.5-m -long hollow core fiber filled with neon gas. Fig. 2A shows the spectra before and after SPM. Chirp mirrors pairs are used to compensate the positively chirp of caused by SPM and material dispersion (exit window, focus lens, etc.) resulting in a few-cycle pulse. The white light pulses are focused into a $0.5\ \text{mm}$ BIBO to generate the $1.2\text{--}2.2\ \mu\text{m}$ seed pulse (Fig. 2B) using intra-pulse different frequency generation (DFG). Intra-pulse DFG is a

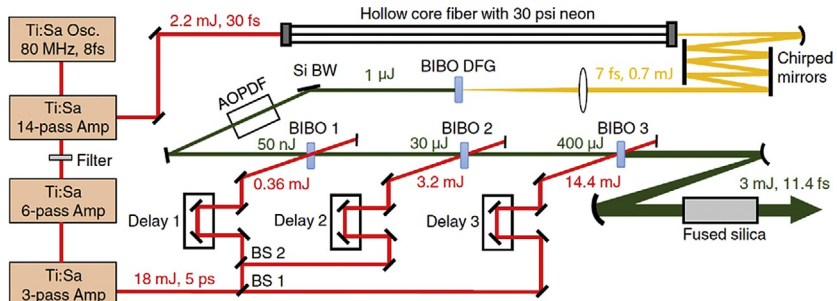


Fig. 1 Schematic setup of the $1.7\ \mu\text{m}$ OPCPA system at UCF. BS1, 20% reflection beam splitter; BS2, 10% reflection beam splitter; Si BW, silicon window at Brewster's angle. AOPDF, acousto-optic programmable dispersive filter for pulse stretching and accurate spectrum phase tuning. Adapted from Yin, Y., Li, J., Ren, X., Zhao, K., Wu, Y., Cunningham, E., Chang, Z., 2016. High-efficiency optical parametric chirped-pulse amplifier in BiB_3O_6 for generation of $3\ \text{mJ}$, two-cycle, carrier-envelope-phase-stable pulses at $17\ \mu\text{m}$. *Opt. Lett.* 41, 1142. <https://doi.org/10.1364/OL.41.001142> © The Optical Society.

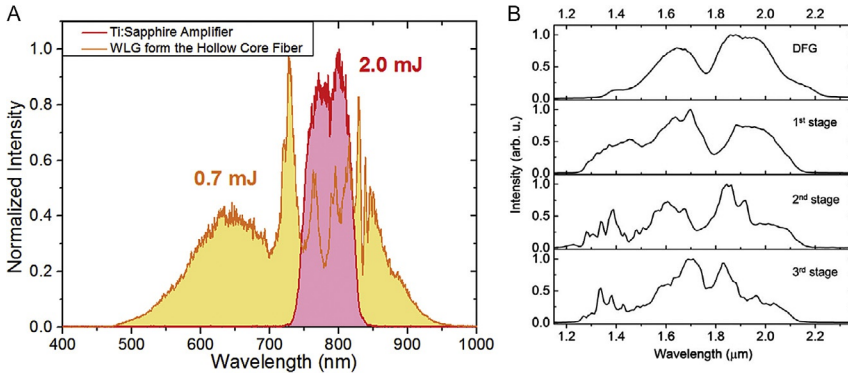


Fig. 2 (A) The Ti:Sapphire amplifier output spectrum for seeding the hollow core fiber (red); White light spectrum after hollow core fiber (yellow). (B) Spectra of OPCA signal beam taken at successive stages. Adapted with permission from Li, J., 2018. *Generation and Characterization of Isolated Attosecond Pulse in the Soft X-ray Regime*; Yin, Y., Li, J., Ren, X., Zhao, K., Wu, Y., Cunningham, E., Chang, Z., 2016. *High-efficiency optical parametric chirped-pulse amplifier in BiB₃O₆ for generation of 3 mJ, two-cycle, carrier-envelope-phase-stable pulses at 17 μm* . *Opt. Lett.* 41, 1142. <https://doi.org/10.1364/OL.41.001142> © The Optical Society.

commonly used method for passively stabilizing the CEP of the SWIR seed (Fuji et al., 2004), which is crucial for driving isolated attosecond pulse generation. The remaining 1.4 mJ pulse from the 14-pass amplifier was spectrally clipped to 760–810 nm before being boosted to 21 mJ in cryo-cooled multi-pass amplifiers. This bandwidth was chosen to pump the BIBO crystal in a non-collinear geometry illustrated later.

The bandwidth of the signal pulse is close to one octave. Angularly dispersive devices such as grating can hardly manage this bandwidth and will, on the other hand, couple mechanical vibration into CEP jitter (Li et al., 2006). Therefore, the stretching and compression of the signal pulses is performed by an acousto-optic programmable dispersive filter (AOPDF) and material dispersion in fused silica bulk, respectively. The AOPDF allows for pre-compensation of high-order phase that would not otherwise be compensated by the fused silica. The signal pulse in the parametric amplifier stretched to ~ 4.4 ps. The 18 mJ pump beam is set to ~ 5 ps to match the seed pulse duration. The CEP values of the signal pulse can be preserved and fine-tuned by the AOPDF.

To separate the signal beam from the pump and idler, the parametric amplification is operated in a noncollinear geometry with a noncollinear angle of $\alpha = 0.6^\circ$ and a phase matching angle of $\theta = 10.8^\circ$ inside the crystal

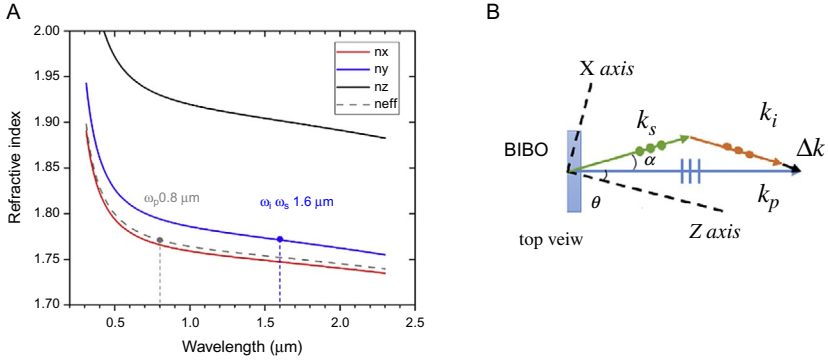


Fig. 3 (A) Optical refractive index of BIBO crystal for type I interaction ($0.8 \mu\text{m}$ (e) \rightarrow $1.6 \mu\text{m}$ (o) + $1.6 \mu\text{m}$ (o)). Refractive index for X, Y and Z-axis is plotted in red, blue and black line. Refractive index for pump wave is plotted in dashed gray line with a phase matching angle of $\theta = 11$ degree. (B) Top view of crystal oriental with respect to the input field polarization. Adapted with permission from Li, J., 2018. *Generation and Characterization of Isolated Attosecond Pulse in the Soft X-ray Regime*.

(Fig. 3B) (Li, 2018). In this case, the modulus of wave vector mismatch Δk can be calculated by:

$$\Delta k = \sqrt{k_p^2 + k_s^2 - 2k_p k_s \cos \alpha} - k_i \quad (7)$$

where k_p , k_s , and k_i are the wavenumbers of the pump, signal and idler beams, respectively. The phase matching efficiency $\text{sinc}^2(\Delta k L / 2)$ as a function of pump and signal wavelength in BIBO crystal is shown in Fig. 4B. The black line represents the actual temporal overlapping of the pump and signal wavelength according to their chirp in the parametric amplifier. The overlap of black line with red region indicates that a good phase matching condition is fulfilled for $1.2\text{--}2.2 \mu\text{m}$. Notice that the symmetry between signal and idler is broken under noncollinear geometry. As can be seen in Fig. 4B that the red area is tilted. This increases the useful bandwidth of pump in the OPCPA and improves the efficiency of CPA laser. The signal spectra in each stage were compared in Fig. 2B. Gain narrowing is eliminated by the broadband phase matching. For such a broad bandwidth, spectral phase up to at least the fourth order need to be tuned carefully to ensure that a two-cycle, 11.4fs pulse is achieved after the bulk compressor (Fig. 5). Without adding active feedback for phase compensation or slow CEP drift, the kHz OPCPA system can run stably for over 8h, which is long enough for data collection in most attosecond experiments.

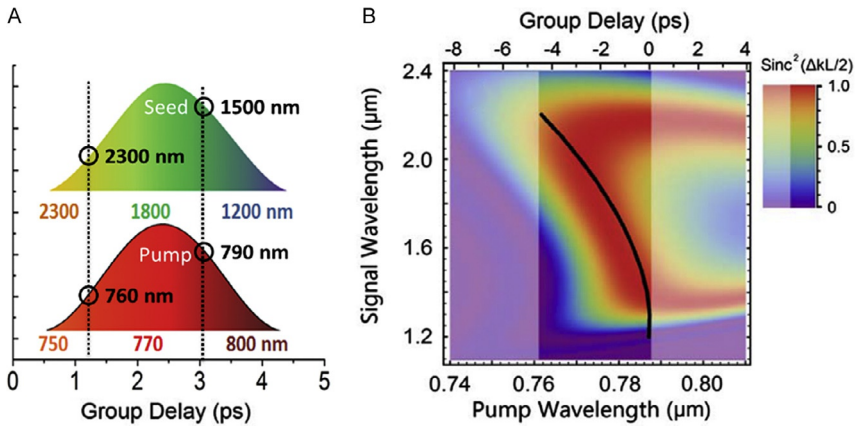


Fig. 4 (A) A schematic illustration of a positively chirped seed (signal) and a negatively chirped pump pulse overlap in time domain. The dashed lines indicate the matched two wavelengths in time. (B) Calculated phase match efficiency ($\text{sinc}^2(\Delta kL/2)$) as a function of pump and signal wavelength in BIBO crystal using the condition $\theta = 10.8^\circ$ and $\alpha = 0.6^\circ$. The black line represents the chirped signal pulse with its corresponding wavelengths marked by the left axis and its temporal chirp marked by the top axis. The chirp of signal and pump pulse in three OPCPA stages are determined by the dispersion in a fused silica rod and grating pairs, respectively. *Adapted with permission from Li, J., 2018. Generation and Characterization of Isolated Attosecond Pulse in the Soft X-ray Regime.; Yin, Y., Li, J., Ren, X., Zhao, K., Wu, Y., Cunningham, E., Chang, Z., 2016. High-efficiency optical parametric chirped-pulse amplifier in BiB₃O₆ for generation of 3 mJ, two-cycle, carrier-envelope-phase-stable pulses at 17 μm . Opt. Lett. 41, 1142. <https://doi.org/10.1364/OL.41.001142> © The Optical Society.*

2.2 Cr:ZnSe chirped pulse amplifier centered at 2.5 μm

An alternative route for high-energy mid-infrared few-cycle systems is to deploy the more conventional technique of chirped pulse amplification (Strickland and Mourou, 1985) in novel laser media. Of particular interest to the attosecond community are transition metal-doped zinc and cadmium chalcogenide compounds, which allows for broadband vibronic lasing at mid-infrared wavelengths. The spectroscopic properties of these materials have been investigated since the end of the 1960s (Vallin et al., 1969), but it was not until the mid-1990s that they were successfully deployed as a gain medium in a laser (DeLoach et al., 1996; Hömmerich et al., 1997; Page et al., 1997). One class of these laser media is the chromium doped chalcogenide compounds, which was extensively reviewed by Sorokina (2004).

The chromium doped zinc selenide (Cr:ZnSe) laser is similar to the Ti:Sapphire laser in many aspects including the broad bandwidth and lifetime of the fluorescence as well as high emission and absorption cross-sections (Sorokina, 2004). In Table 2, the material properties of Ti:Sapphire,

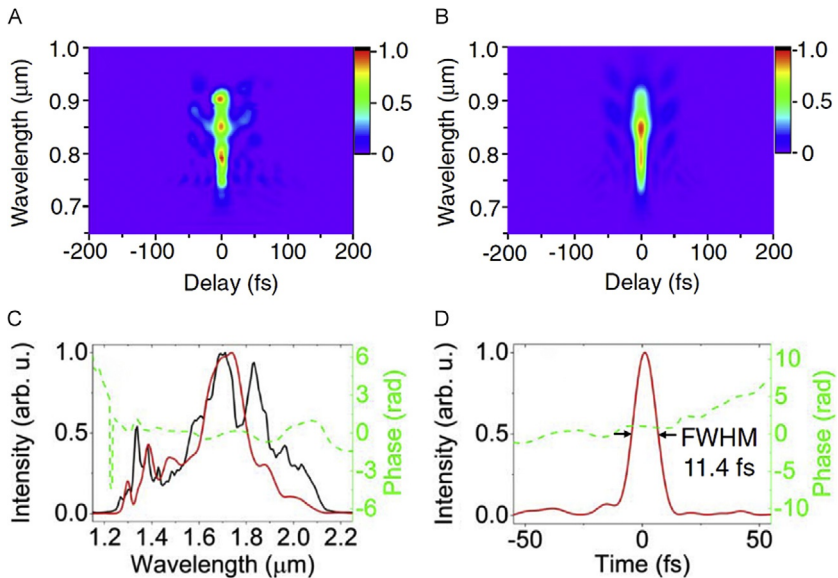


Fig. 5 (A) Experimental SHG FROG trace; (B) retrieved SHG FROG trace; (C) independently measured spectrum (black), retrieved spectrum (red), and retrieved spectral phase (green); (D) retrieved pulse (red) and temporal phase (green). *Adapted with permission from Yin, Y., Li, J., Ren, X., Zhao, K., Wu, Y., Cunningham, E., Chang, Z., 2016. High-efficiency optical parametric chirped-pulse amplifier in BiB₃O₆ for generation of 3 mJ, two-cycle, carrier-envelope-phase-stable pulses at 17 μm. Opt. Lett. 41, 1142. <https://doi.org/10.1364/OL.41.001142> © The Optical Society.*

Yb:YAG and Cr:ZnSe are compared. It is clear by inspection that Cr:ZnSe has the potential to scale like Ti:Sapphire in terms of pulse energy and duration, while the high quantum efficiency minimizes heating issues, which in principle would allow for high repetition rate options for Cr:ZnSe based laser systems. The first high-energy short pulse laser amplifier based on Cr:ZnSe was developed in 2011 by Slobodchikov and Moulton, who demonstrated 300-μJ, 50-nm, 300-fs pulses at a repetition rate of 1 kHz utilizing a Cr:ZnSe oscillator followed by chirped pulse amplification in a regenerative amplifier pumped by a Q-switched holmium-doped yttrium lithium fluoride (Ho:YLF) laser (Slobodchikov and Moulton, 2011). This system was further amplified in two single pass amplification stages up to 1 mJ, 184 fs output pulses in 2016 (Slobodchikov et al., 2016). Earlier this year Vasilyev et al. demonstrated a compact 1.5 mJ, 138 fs system (Vasilyev et al., 2019). This system, which had a footprint of $1.7 \times 1.2 \text{ m}^2$, also contained a chromium-doped zinc sulfide (Cr:ZnS) oscillator followed by chirped pulse amplification in a Cr:ZnSe regenerative amplifier, and was then followed by a single pass Cr:ZnSe power booster stage.

Table 2 Laser parameters for Yb:YAG, Ti:Sapphire, Cr:ZnSe (Anashkina and Antipov, 2010; Durand et al., 2014; Koerner et al., 2012; Major et al., 2004; Sorokina, 2004; Takeuchi et al., 2009).

Material	Ti: Sapphire	Yb: YAG	Cr: ZnSe
Peak emission (nm)	780	1030	2450
Peak absorption (nm)	500	940	1780
Quantum efficiency between peaks (%)	64	91	73
Fluorescence bandwidth (nm)	300	20	900
Peak emission cross-section (10^{-20} cm^{-2})	39–45	2	90–130
Peak absorption cross-section (10^{-20} cm^{-2})	6.5	0.8	87–110
Fluorescence lifetime (μs)	3	850	8
Saturation intensity (kWcm^{-2})	188	11	11
Nonlinear refractive index at lasing wavelength ($10^{-16} \text{ cm}^2 \text{ W}^{-1}$)	5	6.5	80
Thermo-optic coefficient (10^{-6} K^{-1})	12	7.3	70
Diode pumped amplifiers	No	Yes	Yes

At University of Central Florida (UCF) we have also explored the possibility of utilizing Cr:ZnSe as a gain medium for high-energy mid-infrared ultrashort lasers (Ren et al., 2018b; Wu et al., 2019). The laser schemes we have developed are shown in Fig. 6. The minimal pulse duration of a laser pulse is inversely proportional to the spectral bandwidth, due to the uncertainty principle, and for attosecond pulse through HHG it is advantageous to have as short driving laser pulses as possible. So it is important for these lasers to maximize the bandwidth of the laser chain. It is well known that gain narrowing is more severe in a regenerative amplifier than in a multi-pass amplifier (Le Blanc et al., 1996). In order to maximize the bandwidth of our amplified laser pulses we therefore deployed multi-pass amplification schemes in our systems. In order to minimize the overall gain factor, we generate broadband microjoule seed pulses through a technique called intra-pulse difference frequency generation (IDFG) (Yin et al., 2017) as described below.

A 14-pass Ti:Sapphire CPA system is used to generate 1.5 mJ, 30 fs, 800 nm pulses at a repetition rate of 1 kHz. These pulses are spectrally broadened and compressed in a conventional argon-filled hollow-core fiber setup followed by a set of double-angle chirped mirrors. The few-cycle near infrared pulses are focused into a 0.8 mm thick bismuth borate (BIBO) crystal

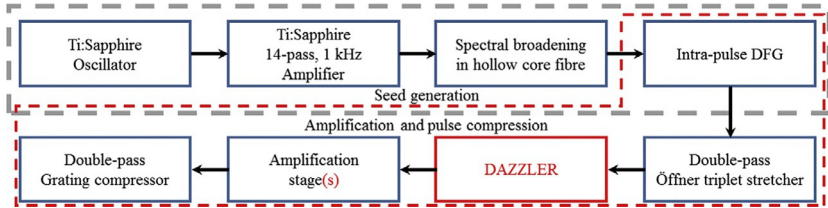


Fig. 6 Overview of the two iterations of laser systems we have developed at UCF. The red font indicates the changes between (Ren et al., 2018b) and (Wu et al., 2019). A DAZZLER was installed, the amplification stages were reduced from 3 to 1, and the entire system starting from the IDFG was rebuilt inside a sealed nitrogen atmosphere.

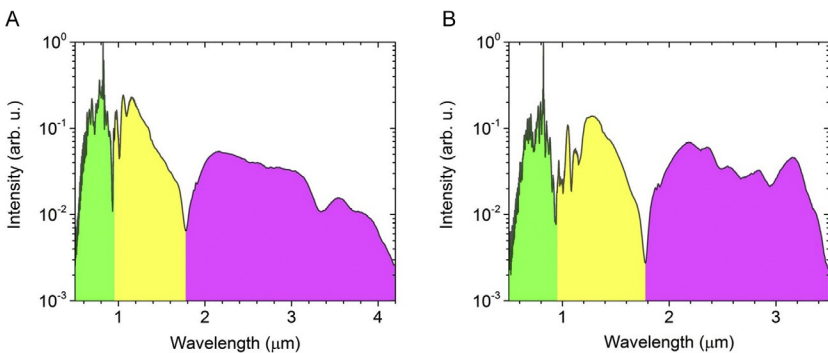


Fig. 7 Measured IDFG output spectrum from (A) 0.4 mm and (B) 0.8 mm BIBO crystals with the input polarization parallel to the ordinary axis of the BIBO crystals. The green shaded area shows the input pulse, while the yellow and magenta area indicates the signal and idler pulses, respectively. This figure was reproduced from Yin, Y., Ren, X., Chew, A., Li, J., Wang, Y., Zhuang, F., Wu, Y., Chang, Z., 2017. Generation of octave-spanning mid-infrared pulses from cascaded second-order nonlinear processes in a single crystal. *Sci. Rep.* 7, 11097. <https://doi.org/10.1038/s41598-017-11652-9> under the Creative Commons Attribution 4.0 License.

cut for type-I phase matching that allows for IDFG. The broad bandwidth of the IDFG process combined with the bandwidth of the few-cycle pump laser allows for a two very broadband down converted pulses to be generated as shown in Fig. 7 (Yin et al., 2017). For a BIBO crystal thickness of 0.8 mm the idler spectrum covers the 1.8–4.2 μm range. A long-pass filter is used to block the signal and seed pulses, while the idler is used a seed pulse for the laser chain. The idler pulse is sent to an aberration free Öffner-triplet stretcher containing a reflective grating with groove density of 300 L/mm. The radius of curvature of the convex and the concave mirror of the Öffner telescope is 1 m and 0.5 m, respectively. The stretched pulse

duration and energy after the stretcher were roughly 300 ps and 3 μJ , respectively. At this point the two iterations of the laser system differs. In the first iteration the amplification was performed in first a six-pass amplifier followed by two single pass amplifiers using Brewster cut polycrystalline Cr:ZnSe crystals (Ren et al., 2018b), while in the second iteration the amplification consisted of a five-pass amplifier in normal incidence cut polycrystalline Cr:ZnSe crystals (Wu et al., 2019).

In both cases the compression was subsequently performed with a double-pass grating compressor. In the initial work we managed to produce 2.3 mJ, 88 fs pulses, while the newer version produced 3.5 mJ, 44 fs pulses. We attribute the enhanced pulse duration performance (Wu et al., 2019) to better dispersion management by the deployment of a mid-infrared acousto-optic programmable dispersive filter, DAZZLER (Maksimenka et al., 2010), and that the laser was built inside a nitrogen purged atmosphere, thus eliminating issues with water vapor in the laser chain. This allowed us to better compress the pulses as shown in Fig. 8.

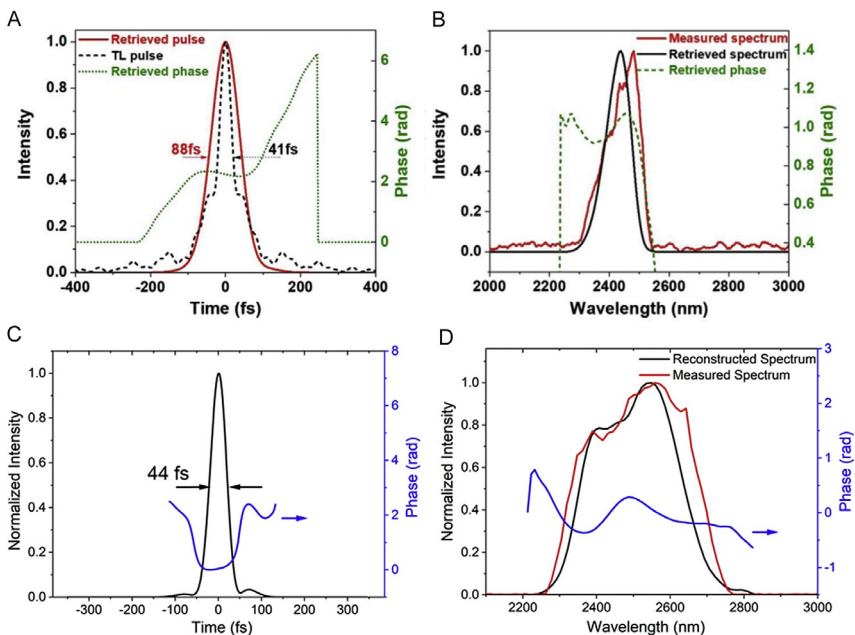
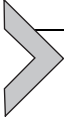


Fig. 8 Output pulse duration and spectrum from the two systems. *The figure was adapted with permission from Ren, X., Mach, L.H., Yin, Y., Wang, Y., Chang, Z., 2018b. Generation of 1 kHz, 23 mJ, 88 fs, 25 μm pulses from a Cr²⁺:ZnSe chirped pulse amplifier. Opt. Lett. 43, 3381. <https://doi.org/10.1364/OL.43.003381> © The Optical Society, and Wu, Y., Zhou, F., Larsen, E.W., Zhuang, F., Yin, Y., Chang, Z., 2019. Generation of 3 mJ, 44 fs, 2.5 micrometer pulses from a single-stage Cr²⁺:ZnSe amplifier. arXiv 1910.06650.*



3. Isolated attosecond pulse generation in the water window

Driving high harmonic generation with long wavelength lasers is an effective approach to extend the cutoff photon energy. However, the amplitude of dipole moment scales unfavorably with laser wavelength, as indicated by

$$I_X(\omega_X) \propto |\tilde{D}(\omega_X)|^2 \propto \left[\frac{\pi}{\varepsilon + i(t_r - t_i)/2} \right]^3 \propto \frac{1}{\lambda^3}, \quad (8)$$

The underlying physical mechanism is quantum diffusion of the electron wave packet during the second step of the HHG process. The recombination cross-section in the third step decreases with the high harmonic photon energy, which also reduces the single atom response in the water window and beyond. This phenomenon was first investigated experimentally in 2001 (Shan et al., 2001). More precise scaling law ($\lambda^{-5\sim-6}$) of single atom response was later discovered (Shiner et al., 2009; Tate et al., 2007). As described below, the weak single atom response in the water window range can be partially compensated by phase matching HHG in gas target with large density-length product since X-ray absorption by the large atoms is low.

3.1 Phase-matched high harmonic generation in the water window

The HHG signal strength achieved in experiment is affected by the phase match condition, where the driving field and the HHG field need to propagate with the same phase velocity to ensure that the HHG field emitted from different atoms buildup coherently (Popmintchev et al., 2009; Rundquist et al., 1998).

The instantaneous phase of a harmonic wave with angular frequency ω and wavelength λ traveling along the z direction of a one-dimensional medium can be described as $\phi(z, t) = kz - \omega t$ by using the physicists' sign convention, where $k = 2\pi/\lambda$ is the wave vector and the phase velocity is $v_\phi = \omega/k$. Apparently, the wave number can be calculated from the phase, i.e., $k = \frac{\partial \phi}{\partial z}$. For a wave propagating in a three-dimensional space, the phase becomes $\phi(\vec{r}, t) = \vec{k} \cdot \vec{r} - \omega t$. The wave vector $\vec{k} = \nabla \phi$, which is the generalization of the expression of k .

The phase matching condition of the X-ray wave generation can be expressed as $\vec{v}_{\phi, \omega_X} - \vec{v}_{\phi, source} = 0$ or $\vec{k}_X - \vec{k}_{source} = 0$, where ω_X , \vec{v}_{ϕ, ω_X} and \vec{k}_X are the angular frequency, phase velocity and wave vector of the X-ray wave. The X-ray wave propagates in the HHG gas target with the speed of light in vacuum, i.e., $v_{\phi, \omega_X} = c$, thus $k_X = \omega_X/c$. $\vec{v}_{\phi, source}$ and $\vec{k}_{source} = \nabla\phi_{source}$ are the phase velocity and wave vector of the polarization wave (source) that produces the X-ray wave. The latter can be decomposed into two contributions $\nabla\phi_{source} = \frac{\omega_X}{\omega_0} \nabla\phi_{IR} + \nabla\phi_{dipole}$ where ω_0 is the angular frequency of the IR driving laser field. The phase of the IR field, ϕ_{IR} , depends on the focusing condition, as well as the spatial distribution of the plasma and neutral gas density. ϕ_{dipole} is the intrinsic single atom dipole phase predicted by the strong field approximation (Salières et al., 1995).

A full three-dimensional determination of the phase matching including propagation effects such as plasma defocusing and laser reshaping is cumbersome (Jin et al., 2018; Johnson et al., 2016). However, it is informative to calculate the phase-matching ignoring these effects. When the X-ray is generated in a uniform target by a plane IR wave, $\nabla\phi_{dipole} = 0$ there is no Gouy phase contribution to $\nabla\phi_{IR}$, therefore $k_{source} = \frac{\omega_X}{\omega_0} \frac{\omega_0}{c} [1 + \Delta n_{neutral}(\omega_0) + \Delta n_{plasma}(\omega_0)]$. The sign of the index of refraction change caused by the neutral gas, $\Delta n_{neutral}$, is opposite to that by the plasma, Δn_{plasma} , at the IR frequency. The two contributions cancel out at certain ionization probability, p_{cr} , of target atom, which leads to perfect phase matching (Rundquist et al., 1998). Here p_{cr} depends on the driving laser wavelength and target element. The so-called phase-matching cutoff can be estimated using Eq. (1) by setting I_0 to the intensity value at which p_{cr} is reached for a given pulse duration, which yield

$$\hbar\omega_c = I_p + \frac{0.5I_p^{3.5}\lambda_{IR}^2}{\left[\ln \left(\frac{0.86I_p 3^{2n^*-1} G_{lm}^2 C_{n^*}^2 \tau_p}{-\ln(1-p_{cr})} \right) \right]^2}, \quad (9)$$

The unit of $\hbar\omega_c$ and ionization potential I_p is eV. The unit of laser wavelength λ_{IR} is μm . The laser pulse duration (FWHM) τ_p is fs. The values of n^* , G_{lm} , and $C_{n^*}^2 L^*$ are found in Chang (2011).

The index of refraction of noble gas in the SWIR and MWIR region can be expressed by the Lorentz Classical Electron Oscillator model with a single resonance frequency ω_r , which leads to $p_c = \left(\frac{2\pi c}{\omega_r \lambda_{IR}} \right)^2$ (Chang, 2011). The pulse duration can also be expressed in term of wavelength,

i.e., $\tau_p = n_{oc} \lambda_{IR} / c$, where n_{oc} is the number of optical cycles fitting into the given pulse duration.

$$\hbar\omega_c = I_p + \frac{0.5 I_p^{3.5} \lambda_{IR}^2}{\left[\ln \left(\frac{2.87 I_p^{3.2n^* - 1} G_{lmc}^2}{- \lambda_{IR} \ln \left(1 - \left(\frac{1.88}{\omega r \lambda_{IR}} \right)^2 \right)} \right) \right]^2}, \quad (10)$$

which shows the explicit dependence of the phase-matching cut-off photon energy on the driving laser wavelength. The unit of ω_r is given in rad/fs.

Fig. 9 shows the calculated HHG cutoff from different driving laser wavelengths using Eq. (10), i.e., under perfect phase matching condition where the plasma induced index of refraction and that of the neutral target gas is well balanced (Rundquist et al., 1998). A few-cycle laser pulse with wavelength $> 1.6 \mu\text{m}$ is enough to produce water window harmonics from neon and helium gas.

The ionization probability to achieve perfect phase matching for helium atom and a plane-wave driving laser centered at $2 \mu\text{m}$ is $p_{cr} = 8 \times 10^{-4}$, which indicates that the three-step HHG process occurs in less than 1/1000 of the

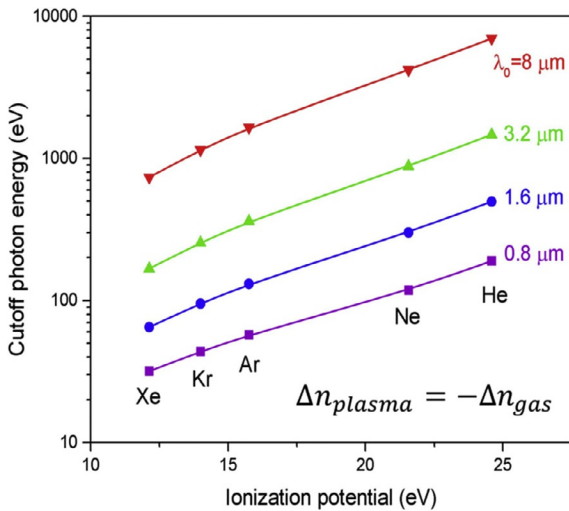


Fig. 9 Calculated phase matched cutoff of high harmonic generation from various inert gases driven by lasers at different wavelengths. Adapted with permission from Ren, X., Li, J., Yin, Y., Zhao, K., Chew, A., Wang, Y., Hu, S., Cheng, Y., Cunningham, E., Wu, Y., Chini, M., Chang, Z., 2018a. Attosecond light sources in the water window. *J. Opt.* 20, 023001. <https://doi.org/10.1088/2040-8986/aaa394>.

target atoms. The value becomes even smaller for longer wavelength lasers. Mechanisms for phase matching at higher ionization probability have also been investigated (Geissler et al., 2000). When the three-dimensional distribution of a focused Gaussian-type laser field is taken into consideration, the instantaneous intensity $I_{IR}(\tau, z)$ and phase $\phi_{IR}(\tau, z)$ of the driving lasers in the gas target can be calculated by solving the nonlinear wave-propagation equation in a moving frame where $\tau = t - z/c$. The phase mismatch along the propagation axis can be described by

$$\Delta k(\tau, z) = -\frac{\omega_X}{\omega_0} \partial_z \phi_{IR}(\tau, z) - \partial_z \phi_{dipole}(\tau, z), \quad (11)$$

where $\phi_{IR}(\tau, z) = \frac{\omega_0}{c} [\Delta n_{neutral}(\omega_0, \tau, z) + \Delta n_{plasma}(\omega_0, \tau, z)]z + \phi_f(\omega_0, \tau, z)$. The term $\phi_f(\omega_0, \tau, z)$ includes Gouy phase and plasma defocusing effects. The dipole phase $\phi_{dipole}(\tau, z) = -\alpha U_p(\tau, z)/\hbar\omega_0$, where $\alpha \approx 3$ for the short trajectory, $U_p[eV] = 9.22\lambda_{IR}[\mu m]^2 I_{IR}[10^{14} W/cm^2]$ is the ponderomotive potential. When the plasma induced frequency blue shift of the driving laser is considered, $\partial_z \phi_{dipole}(\tau, z) = -\frac{\alpha}{\hbar} \left[\frac{1}{\omega_0} \partial_{I_{IR}} U_p \partial_z I_{IR} + \partial_{\omega_{IR}} \left(\frac{U_p}{\omega_{IR}} \right) \partial_z \omega_{IR} \right] = -\alpha \frac{U_p}{\hbar\omega_0} \left[\frac{\partial_z I_{IR}(\tau, z)}{I_{IR}(\tau, z)} - 3 \frac{\partial_z \omega_{IR}(\tau, z)}{\omega_{IR}(\tau, z)} \right]$ (Schötz et al., 2019), therefore the phase-mismatch becomes

$$\begin{aligned} \Delta k(\tau, z) = & -\frac{\omega_X}{\omega_0} \partial_z \left[\frac{\omega_0}{c} [\Delta n_{neutral}(\omega_0, \tau, z) + \Delta n_{plasma}(\omega_0, \tau, z)]z + \phi_f(\omega_0, \tau, z) \right] \\ & + \alpha \frac{U_p}{\hbar\omega_0} \left[\frac{\partial_z I_{IR}(\tau, z)}{I_{IR}(\tau, z)} - 3 \frac{\partial_z \omega_{IR}(\tau, z)}{\omega_{IR}(\tau, z)} \right], \end{aligned} \quad (12)$$

It has been pointed that the decrease of IR intensity in the propagation direction, $\partial_z I_{IR} < 0$, and a blue shift of the driving laser $\partial_z \omega_{IR} > 0$ can counteract the plasma dispersion $-\Delta n_{plasma} = \frac{e^2 N_e}{2\epsilon_0 m_e \omega_0^2} > 0$, which may enable phase-matching the generation of an isolated attosecond pulses significantly above p_{cr} (Schötz et al., 2019). Here e and m_e are the charge and mass of an electron, respectively, and ϵ_0 is the vacuum permittivity and N_e is plasma density.

Recent development of high energy, high repetition rate SWIR lasers base on OPA/OPCPA technique have enabled the generation of water window high harmonic sources with sufficient photon flux for time resolved experiments. High photon flux of isolated attosecond pulses in the water window has been obtained using different approaches a semi-infinite cell

Table 3 Cutoff photon energies that extend beyond carbon K-edge from kHz infrared laser systems.

Infrared laser systems	Generation gas	Cutoff energy (eV)	Year
1.5 μm , 1.6 mJ, 50 fs	Neon	400	2009 (Xiong et al., 2009)
1.6 μm , 0.55 mJ, 9 fs	Neon	320	2014 (Ishii et al., 2014)
1.8 μm , 0.7 mJ, 8 fs	Neon	375	2016 (Johnson et al., 2016)
1.85 μm , 0.4 mJ, 12 fs	Neon (helium)	350(500)	2016 (Teichmann et al., 2016)
2.1 μm , 1.35 mJ, 32 fs	Neon	450	2016 (Stein et al., 2016)
1.7 μm , 1.5 mJ, 12 fs	Neon	450	2016 (Li et al., 2016)
1.8 μm , 0.55 mJ, 12 fs	Helium	600 eV	2018 (Johnson et al., 2018)

Adapted from Ren, X., Li, J., Yin, Y., Zhao, K., Chew, A., Wang, Y., Hu, S., Cheng, Y., Cunningham, E., Wu, Y., Chini, M., Chang, Z., 2018a. Attosecond light sources in the water window. *J. Opt.* 20, 023001. <https://doi.org/10.1088/2040-8986/aaa394>.

filled with helium gas with relative low density (Saito et al., 2019), and tight focusing into a high-density helium gas jet (Johnson et al., 2018). Table 3 list some high harmonics source with photon energy extending beyond the carbon K-edge from various OPA/OPCPA system at kHz repetition rate (Ren et al., 2018a).

3.2 Sub-cycle gating techniques for isolated attosecond pulse

A variety of time-resolved measurement, such as attosecond transient absorption spectroscopy (Goulielmakis et al., 2010; Wang et al., 2010) or photoelectron detection (Itatani et al., 2002; Schultze et al., 2010), prefer single isolated attosecond pulses (IAPs). Various gating techniques have been developed to obtain IAPs from the high harmonics pulse train and some of them have been implemented to generate IAPs in the water window. It is quite challenging to generate water window IAPs with high enough photon flux for time resolved experiments.

The generation of isolated attosecond pulse always favors a short driving pulse. However, the amplification bandwidth of typical rare earth gain medium is limited to about one octave and a post-amplified laser pulse usually ends up containing multiple cycles. Even broadband OPA/OPCPA can hardly support single-cycle laser pulses. To isolate a single attosecond burst from a multicycle driving laser, the most straightforward way is amplitude gating (AG) (Hentschel et al., 2001). In AG, the strongest half-cycle of the driving pulse will lead to the brightest attosecond burst whose photon energy exceeds that of the neighbor bursts. Weaker half-cycle of the driving field will still generate photon with lower photon energy. As a result, harmonic peaks are produced by the spectral interference at lower energy side. Proper filters are needed to select the cutoff spectrum that is generated by the strongest half-cycle.

Recently, AG has been adapted in the few-cycle short-wave infrared laser to demonstrate water window IAP (Cousin et al., 2017; Ishii et al., 2012, 2014; Teichmann et al., 2016). An example of the dependence of harmonic cutoff on the CEP for a 1.9-cycle pulses at 1.85 μm laser is shown in Fig. 10A. For a few-cycle pulse, the AG works well because neighboring peaks strength differs significantly. However, for a multicycle pulse, the difference between cutoff energy from neighboring peaks is small, which limits the bandwidth of the attosecond continuum and increases the difficulty of selecting a proper filter. Therefore spectral filtering idea of AG is often combined with other gating methods such as ionization gating (IG) (Abel et al., 2009; Ferrari et al., 2010) and two color gating (Mauritsson et al., 2006; Takahashi et al., 2013).

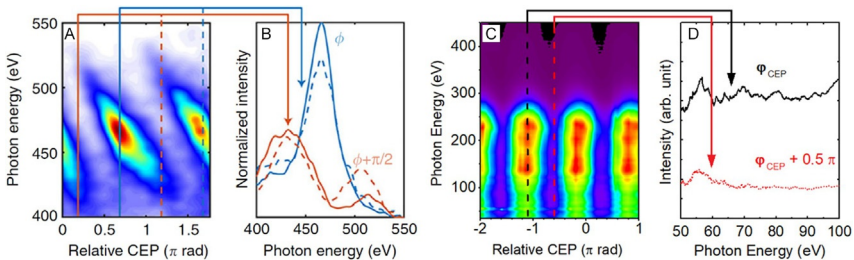


Fig. 10 CEP influence on the attosecond supercontinua in the water window by using AG (A, B) and PG (C, D). Panels (A) and (B) adapted from Teichmann, S.M., Silva, F., Cousin, S.L., Hemmer, M., Biegert, J., 2016. 0.5-keV Soft X-ray attosecond continua. *Nat. Commun.* 7, 11493. <https://doi.org/10.1038/ncomms11493>, and Panels (C) and (D) adapted with permission from Li, J., Ren, X., Yin, Y., Cheng, Y., Cunningham, E., Wu, Y., Chang, Z., 2016. Polarization gating of high harmonic generation in the water window. *Appl. Phys. Lett.* 108, 231102. <https://doi.org/10.1063/1.4953402>.

To overcome the bandwidth limitation from AG and IG, techniques based on the temporal “on and off” switching of the HHG process were developed to generate IAPs with broad spectrum. The most common temporal gating method is the polarization gating (PG) (Chang, 2005; Corkum et al., 1994; Shan et al., 2005; Sola et al., 2006). To compose the PG field, two counter rotating circularly polarized fields overlap collinearly. The resulting PG driving field is near linearly polarized in the middle of the pulse duration and elliptically polarized elsewhere. Illuminated by an elliptically polarized driving field, the freed electron will accumulate a transverse displacement and reduce the recollision probability with its parent ion. As a result, attosecond burst only occurs in the linearly polarized field which is less than half of an optical cycle.

The invention of double optical gating (DOG) technique (Chang, 2007; Mashiko et al., 2008) follows the same principle of PG, in DOG, a second harmonic field is added to the break the fundamental field’s symmetry and increase the interval of the attosecond pulse train. The corresponding gate width of PG can be doubled to a full optical cycle. This will lower the leading-edge field intensity and reduce the ground state depletion before the center linearly polarized fields generates the IAP. Therefore, a stronger IAP with better phase match condition can be expected by using the DOG (Li et al., 2019). In a long wavelength driving field, the recombination of tunneled electron is largely affected by the field ellipticity. Therefore, PG and DOG become more efficient to generate IAPs with long wavelength drivers (Li et al., 2019, 2017).

Another type of gating method relies on spatially separating each attosecond burst, known as the spatiotemporal gating or the “attosecond lighthouse” (Vincenti and Quéré, 2012). This is realized by using pulse front tilt, i.e., a spatially chirped pulse with a wavefront that gradually changes its direction in time. The corresponding attosecond bursts propagate along the direction of the instantaneous wavefront in each half cycle and separate themselves in the far field. This method was first demonstrated from a plasma mirror (Wheeler et al., 2012) and then applied to generated the first water window IAP from the neon gas (Silva et al., 2015). To implement the attosecond lighthouse technique, a higher CEP stability is required since the pointing of the each IAP is coupled with CEP jitter. A method very similar to the attosecond lighthouse technique is called noncollinear optical gating (Louisy et al., 2015). In noncollinear optical gating the driving laser is spatially split in two halves and recombined at a crossing angle with a small delay between the two. This leads to a time dependent pulse front tilt in a

similar manner to the lighthouse and allows for single attosecond pulse generation from multicycle pulses. This method has not yet been implemented for water window harmonics.

3.3 Atto-chirp compensation

The attosecond pulses from high harmonic generation are intrinsically chirped. The electron motion along the short trajectory emits attosecond pulses with positive chirp and long trajectory yield a negative chirp. The different signs of atto-chirp arise from the high harmonic generation process. In X-ray emissions from HHG, only the short trajectory can be phase matched along the propagation axis. The value of the atto-chirp at the center of the plateau region of the high harmonic spectrum can be estimated by using the semi-classical three-step model (Chang, 2011).

$$\text{Chirp} = 1.63 \times 10^{18} \frac{1}{I_0 \lambda_0} \quad (13)$$

where the unit of the chirp is in as^2 . I_0 is the peak intensity of the driving laser in W/cm^2 , and λ_0 is the center wavelength of driving laser in μm . The chirp is 1920 as^2 for a $1.7 \mu\text{m}$ driving laser with an intensity of $5 \times 10^{14} \text{ W}/\text{cm}^2$.

The positive chirp of the attosecond pulses in the wavelength below 300 eV can be compensated by the negative group delay dispersion of thin metallic filters. Fig. 11 shows the transmission and group delay dispersion of

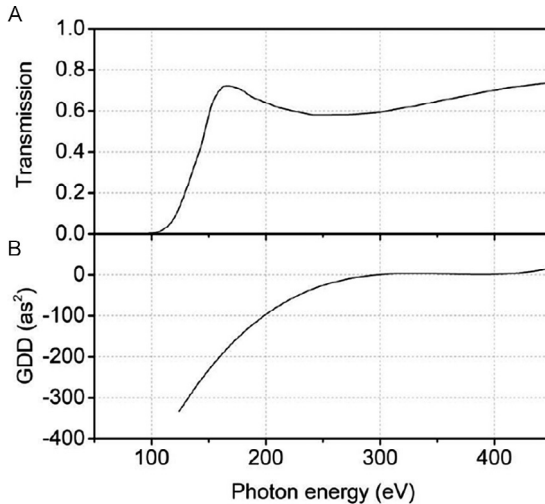


Fig. 11 Calculated transmission (A) and group delay dispersion (B) of 100 nm Sn filter.

100 nm Sn filter. Since the value of group dispersion of Sn filter approaches zero at 300 eV, the positive atto-chirp compensation is only possible below 300 eV. Recently, isolated attosecond pulses around the Carbon K-edge (282 eV) has been realized where the atto-chirp is compensated by Sn thin films of 400 nm thickness (Li et al., 2017).

However, for compensation the atto-chirp beyond 300 eV, it is hard to find appropriate materials that have sufficient dispersion with high transmission. Chirped multilayer mirrors (Guggenmos et al., 2013) and grating stretcher (Poletto et al., 2008) with high negative group delay dispersion can be designed and reduce the positive chirp but the bandwidth is narrow and the reflectivity is low. Recently, atto-chirp compensations by dispersion of plasma was demonstrated by numerical simulations for broadband X-ray attosecond pulses in the water window (282–533 eV) with low loss (Chang, 2018). Unionized hydrogen gas with the proper pressure-length product can reduce the positive chirp partially in the 530–1000 eV (Chang, 2019).

The group delay dispersion of a plasma is

$$GDD(\hbar\omega_X) = -\frac{e^2\hbar^3}{\epsilon_0 m_e c} \frac{N_e L_p}{(\hbar\omega_X)^3} \quad (14)$$

where \hbar is the reduced Planck constant and ω_X is the angular frequency of the X-ray. N_e is the number density of electrons, and L_p is the length of plasma column. The electron density-length product determines the GDD value.

A standard gas at 1 atm pressure and room temperature has the number density of electrons of $2.5 \times 10^{19}/\text{cm}^3$. The number density of electrons of fully ionized 1 atm H_2 gas is thus $5 \times 10^{19}/\text{cm}^3$. Such plasma can induce the GDD of -599 as^2 with $L_p = 10 \text{ cm}$ at $\hbar\omega_X = 300 \text{ eV}$. It can compensate the positive chirp of the attosecond pulses in water window arising from high harmonic generation. The absorption or reflectivity of hydrogen plasma is almost zero for X-ray pulses at 300 eV (Chang, 2018). Fig. 12 shows calculated electric fields of the attosecond X-ray pulses in time domain with/without the chirp compensation by plasma dispersion. The intrinsic positive chirp of the attosecond X-ray pulses can be attuned by hydrogen plasma with proper electron density-length product, which can compress the attosecond pulse duration close to the transform-limited value.

For the atto-chirp compensation by unionized neutral hydrogen molecules, the GDD of a neutral hydrogen gas is

$$GDD(\hbar\omega_x) = -\frac{e^2\hbar^3}{\epsilon_0 m_e c} \frac{N_e L}{(\hbar\omega_x)^3} \quad (15)$$

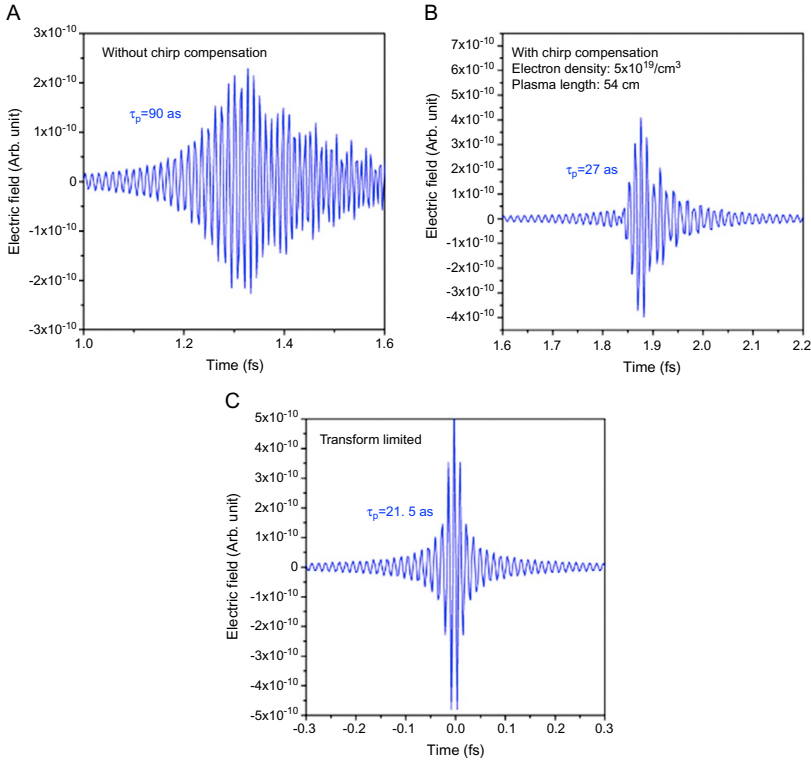
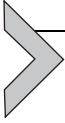


Fig. 12 Electric field profiles of attosecond X-ray pulses in time domain. (A) Without chirp compensation. (B) With chirp compensation of plasma dispersion. (C) Transform-limited pulse. The pulse durations are the full width half maximum of the intensity profiles. Adapted with permission from Chang, Z., 2018. Attosecond chirp compensation in water window by plasma dispersion. *Opt. Express* 26, 33238. <https://doi.org/10.1364/OE.26.033238>

The only difference with the GDD of the plasma is that the length of the plasma is replaced by the length, L , of hydrogen gas column. In the case of hydrogen gas, the number densities of electron of the fully ionized plasma and unionized neutral hydrogen gas are same. The neutral hydrogen gas column with identical length can compensate the positive GDD same with the plasma dispersion column. The neutral gas has lower transmission than plasma. However, it is easier to implement the chirp compensation than plasma dispersion since ionizing the gas with discharge require high voltage and current.



4. Characterization of attosecond X-ray pulses

It is difficult to measure the temporal profile of an isolated attosecond X-ray pulses directly with conventional detector since the electric field oscillates too fast. An attosecond pulses can be characterized by measuring the spectrum and the spectral phase. The spectrum can be measured easily by X-ray grating spectrometers and the spectral phase can be unveiled by the attosecond streaking technique. The attosecond streak camera converts temporal information to momentum information which can be measured by time of flight (TOF) spectrometers. Retrieving the spectral phase will enable a complete characterization of the X-ray pulse in both time- and frequency-domain. This phase retrieval task has long been solved with FROG-CRAB and its derived algorithms (Chini et al., 2010; Mairesse and Quéré, 2005) adapted from frequency-resolved optical gating (FROG), a technique commonly used for femtosecond pulse retrieval. However, attosecond pulse retrieval in the water window is intrinsically plagued by the low photon flux of X-ray pulse and low quantum efficiency in photoelectron emission (Wang et al., 2009), both contributing to large shot noise on the streaking trace. The poor signal-to-noise ratio (SNR) of the measured streaking trace can be compensated by increasing the collection solid angle (Mauritsson et al., 2006; Wang et al., 2009), but the resulting smearing effect on the trace needs to be considered for high fidelity pulse reconstruction. In addition, phase retrieval of ultra-broadband X-ray pulses requires a more complete theoretical modeling of the photoelectron wave during the streaking process, including its momentum and angular distribution, as well as its interaction with the laser field (Ivanov and Smirnova, 2011). Until recently, there has not existed a single pulse retrieval method that can both model the effect of experimental noise on the error and uncertainty of the pulse retrieval, as well as incorporate a complete description of the streaking process. This section summarizes recent advances in attosecond pulse retrieval, with the goal of illustrating how learning-based pulse retrieval handles the challenges facing conventional FROG-derived attosecond pulse retrieval methods.

4.1 Attosecond streaking and FROG-derived attosecond pulse retrieval

The conventional streak camera operates based on converting time-varying information of the signal into spatial information. A picosecond streak

camera consists of a photocathode, a deflection plate, and a phosphor screen. When an unknown optical pulses are incident on the photocathode through a slit, a narrow beam of electron pulses is emitted in to vacuum then imaged on the phosphor screen by the deflection plate (Bradley et al., 1971). Since the photoelectron conversion is considered to be instantaneous, the electron pulses can be regarded as a replica of the unknown optical fields. A linearly ramped voltage on the deflection plates can sweep the electron across the phosphor screen, which make different temporal portion of the electron pulses are displaced at different positions on the screen. One can measure the electron pulses profile with a known sweeping rate and thus one can determine the optical pulses profile. For measuring attosecond pulses, a well-defined oscillating electric field could operate like the sweeping voltage (Fig. 13).

In an attosecond streak camera, an unknown attosecond X-ray pulse and a phase-locked IR pulse are focused into the neutral gas with a relative delay. The delay can be controlled well by piezo stages. The streaking trace is a series of photoelectron spectra $\gamma\left(\left|\vec{k}\right|, \tau\right)$ generated from the interaction between an attosecond X-ray pulse $E_X(t)$ and a femtosecond infrared (IR) pulse $E_{IR}(t)$ in a gaseous medium at various time delays τ . Both X-ray and IR pulses are polarized along the axis of time-of-flight (TOF) spectrometer. Once the gas atoms with ionization potential I_p absorb the energy from an X-ray pulse, photoelectrons with momentum \vec{k} (and hence kinetic energy $W = \left|\vec{k}\right|^2/2$) are produced via dipole transition $d\left(\vec{k}\right)$. The dressing IR field introduces a momentum shift to the photoelectrons, which is

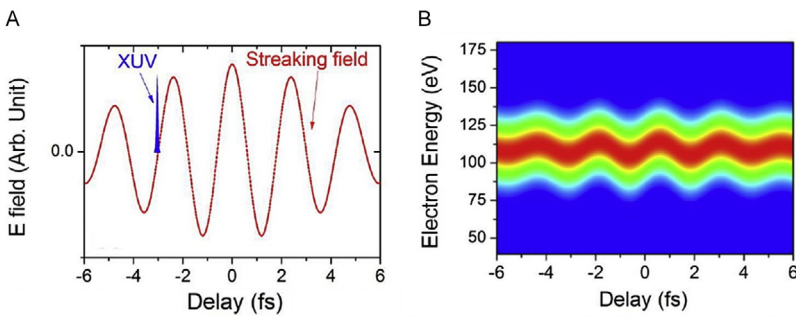


Fig. 13 The principle of attosecond streak camera. (A) Unknown XUV pulse (blue) and known phase-locked IR pulse (red). (B) The streaking trace obtained by tuning of the delay between the XUV and the IR pulses.

manifested in the form of a phase modulation, ϕ_G , on the photoelectron wave packet. The spectrogram $S(\vec{k}, \tau)$ is described by Eq. (16) in atomic units

$$S(\vec{k}, \tau, \theta) = \left| \int_{-\infty}^{\infty} E_X(t - \tau) d_{\vec{k}}^- \exp(i\phi_G(\vec{k}, t)) \exp(i(W + I_p)t) dt \right|^2 \quad (16)$$

$$\phi_G(\vec{k}, t, \theta) = - \int_t^{\infty} \left(|\vec{k}| |A(t')| \cos \theta + |A(t')|^2 / 2 \right) dt', \quad (17)$$

where $A(t) = - \int_{-\infty}^t E_{IR}(t') dt'$ is the vector potential of the IR field along the TOF spectrometer; θ is the observation angle between the photoelectron momentum, \vec{k} , and the TOF axis. If we assume the angular distribution of the photoelectron is $f(\theta)$ against the TOF axis, the ideal streaking trace, I , expressed in terms of photoelectron energy W and delay τ between XUV and dressing IR pulse, is the integral over all the directions of \vec{k} that fall within the maximum collection angle θ_{\max} of the TOF spectrometer

$$I(W, \tau) = \int_{\theta=0}^{\theta_{\max}} S(\vec{k}, \tau, \theta) f(\theta) \sin(\theta) d\theta. \quad (18)$$

Experimentally obtained traces typically contain shot noise due to the low photoelectron flux. If the ideal trace (Eq. 18) is normalized by its maximum intensity, and the experimental average peak count of the trace is λ , for each energy channel W and delay τ , the measured count γ on the trace follows Poisson statistics

$$p(\gamma|I) = \frac{(\lambda I)^\gamma \exp(-\lambda I)}{\gamma!}, \quad (19)$$

where the parameter λ is determined by the photoelectron flux and the integration time.

Under central momentum approximation (Wang et al., 2009), the energy bandwidth of the induced photoelectron is assumed to be much narrower than the central energy. The photoelectron energy can thus be approximated by $W_0 = |\vec{k}_0|^2 / 2$, where \vec{k}_0 is the central momentum of the photoelectrons, and the dipole transition element $d_{\vec{k}}^-$ can be considered as a constant. Moreover, if the angular collection range of TOF spectrometer

is limited, the observation angle θ can be treated as a constant θ_0 , i.e., $f(\theta) = \delta(\theta - \theta_0)$. With these two assumptions, and combine Eqs. (17) and (18), the streaking trace can thus be expressed as a Fourier transform on the product between delayed X-ray pulse and the phase modulation

$$I(W, \tau) = \left| \int_{-\infty}^{\infty} E_X(t - \tau) G(t) \exp(i(W + I_p)t) dt \right|^2 \sin(\theta_0). \quad (20)$$

where

$$G(t) = \exp \left[-i \int_t^{\infty} \left(\sqrt{2W_0} A(t') \cos \theta_0 + |A(t')|^2 / 2 \right) dt' \right] \quad (21)$$

is a temporal phase gate on the photoelectron wavepacket.

Eq. (20) describes the measurement principle behind frequency-resolved optical gating for complete reconstruction of attosecond bursts (FROG-CRAB), which has the same form as the FROG trace in conventional femtosecond pulse characterization. The FROG-CRAB retrieval is thus similar to the principal component generalized projections algorithm (PCGPA) used in blind-FROG (Kane et al., 1997) for retrieving both the signal and unknown gating pulse. This algorithm Fourier transforms back and forth between the time domain and frequency domain, looking for a pair of fields (E_X, G) that satisfies the outer product form in time domain, and the known X-ray spectrum in frequency domain (Kane, 1999).

The central momentum assumption in FROG-CRAB conveniently offers a Fourier transform form of the streaking process that fits in the scope of PCGPA, but at the expense of limited XUV pulse bandwidth it can characterize. This assumption has proven inadequate for characterizing the attosecond pulses generated from the double optical gating and polarization gating (Mashiko et al., 2009; Sansone et al., 2009), which can produce ultra-broad pulses with durations on tens of attoseconds. In this case, the dependence of the phase modulation on the photoelectron momentum (Eq. 17) has to be considered. This yields a phase gate that is a function of both energy W and time t ,

$$G(W, t) = \exp \left[-i \int_t^{\infty} \left(\sqrt{2W} A(t') \cos \theta_0 + |A(t')|^2 / 2 \right) dt' \right]. \quad (22)$$

and the ideal streaking trace is expressed by

$$I(W, \tau) = \left| \int_{-\infty}^{\infty} E_X(t - \tau) G(W, t) \exp(i(W + I_p)t) dt \right|^2 \sin(\theta_0). \quad (23)$$

The second harmonic component of Eq. (23) describes the measurement principle of PROOF (Chini et al., 2010). By obviating the central momentum assumption in FROG-CRAB, PROOF is capable to characterize traces shorter than atomic unit of time, yet it falls beyond the scope of PCGPA, which requires a gate pulse independent on energy. The pulse retrieval from PROOF trace has been implemented with genetic algorithm (Baumert et al., 1997), which seeks X-ray spectral phases (represented as “chromosomes” in $0 \sim 2\pi$) that minimize the mean square error between the second harmonic component of the measured trace and reconstructed trace from guessed phase angles.

To improve the fidelity of reconstructed attosecond pulse, and lower the limit on retrievable pulse duration further below atomic unit of time, more accurate description of the streaking process should be incorporated in the pulse retrieval algorithm. Toward this end, the angular distribution of the photoelectron has been considered in the streaking process (Gaumnitz et al., 2018). Instead of using a delta function to simplify $f(\theta)$, the angular distribution is more accurately represented by

$$f(\theta) = 1 + \frac{\beta}{2} (3 \cos^2 \theta - 1), \quad (24)$$

where β is a parameter that accounts for the asymmetry distribution of the ionized photoelectrons (Kennedy and Manson, 1972). The complete streaking trace is thus

$$I(W, \tau) = \int_0^{\theta_{\max}} \left| \int_{-\infty}^{\infty} E_{XUV}(t - \tau) G(W, t, \theta) \exp(i(W + I_p)t) dt \right|^2 f(\theta) \sin(\theta) d\theta, \quad (25)$$

where the phase gate G depends on both energy and the observation angle

$$G(W, t, \theta) = \exp \left[-i \int_t^{\infty} \left(\sqrt{2W} A(t') \cos \theta + |A(t')|^2 / 2 \right) dt' \right] \quad (26)$$

The inclusion of photoelectron angular distribution in the streaking process opens up the opportunity to allow a larger angular range collected by the detector, thus also improving the signal-to-noise ratio (SNR) of the measured streaking trace. The pulse retrieval from Eq. (25) employs the Volkov transform generalized projection algorithm (VTGPA) (Gaumnitz et al., 2018; Keathley et al., 2016). Different from PCGPA, which enforces the outer product in time domain, VTGPA minimizes the mean square error between the measured and reconstructed streaking trace with a gradient-based search for the optimal time-domain amplitude and phase of $E_X(t)$ and $A(t)$.

Fig. 14 is a schematic illustration for generation and characterization of isolated attosecond pulses with streak camera technique (Li et al., 2017). In this case, the driving IR laser pulses have pulse energy of 1.5 mJ, pulse duration of 12 fs, and stabilized CEP. The driving IR laser pulses is split into two arms, X-ray generation arm and dressing IR laser field. Most of pulse energy (>80%) goes to the X-ray generation arm then passes through polarization optics for the gating of isolated attosecond pulses. The pulse energy and beam size at X-ray generation can be controlled by an iris and focus lens. The focused pulses generate isolated attosecond pulses in soft X-ray regime by high harmonic generation. The focused pulses generate isolated attosecond pulses in soft X-ray regime by high harmonic generation.

To characterize the generated isolated attosecond pulses, well-defined IR pulses are combined to the attosecond pulses by a mirror with a hole (Li et al., 2017) or a two-part mirror (Fabris et al., 2015) mounted on a piezo controlled stage for delay control. The delayed two pulses are focused onto an effusive gas target positioned at the entrance of an electron TOF spectrometer. Photoelectron spectra are recorded as a function of the time delay

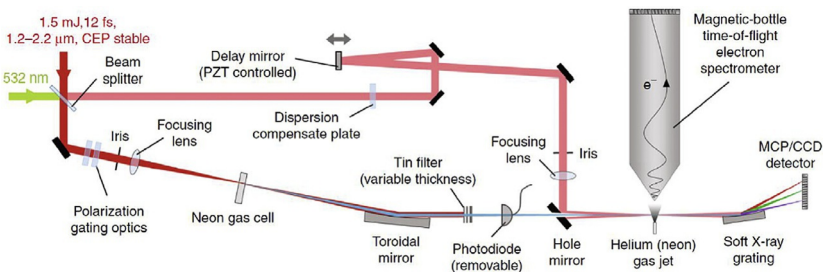


Fig. 14 Experimental setup for attosecond streaking camera. Adapted with permission from Li, J., Ren, X., Yin, Y., Zhao, K., Chew, A., Cheng, Y., Cunningham, E., Wang, Y., Hu, S., Wu, Y., Chini, M., Chang, Z., 2017. 53-attosecond X-ray pulses reach the carbon K-edge. *Nat. Commun.* 8, 186. <https://doi.org/10.1038/s41467-017-00321-0>.

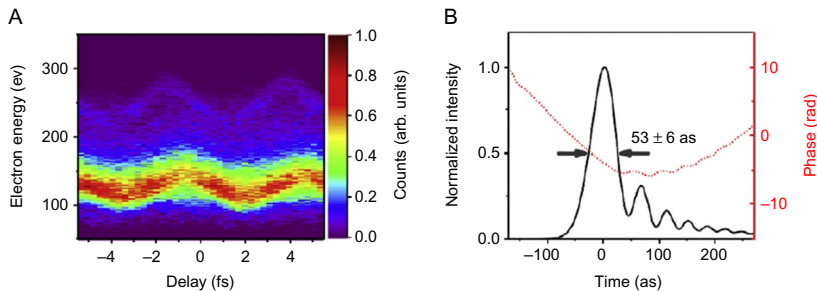


Fig. 15 Photoelectron spectrogram from attosecond streaking camera and retrieval of the attosecond pulses. (A) Photoelectron spectrogram as a function of temporal delay between the attosecond pulses and the IR pulses. (B) Retrieved temporal profile and phase of the attosecond pulses by PROOF method.

between the unknown X-ray attosecond pulses and the well-defined IR pulses. Fig. 15 shows the measured photoelectron spectra of 53 attosecond pulses. The streaking camera recorded the photoelectron spectra and it was retrieved by phase retrieval by omega oscillation filtering (PROOF) (Chini et al., 2010).

4.2 Attosecond pulse retrieval with neural networks

Despite efforts to refine the attosecond streaking model used in pulse retrieval algorithms, complete descriptions on the interaction between photoelectron and IR laser field have not been fully included (Ivanov and Smirnova, 2011). Implementing these interactions necessitates modeling the dipole transition element d as energy- or time-dependent, and is destined to bring more complexity to the current retrieval algorithms, making them more time-consuming. Moreover, the output of these algorithms is typically a deterministic solution of the XUV and IR pulse pair, given an input streaking trace. The effects of experimental noise on the error and uncertainty of the retrieved pulse cannot be easily studied with existing algorithms because this requires an algorithm that can output all possible solutions given a noisy trace.

Neural networks have seen increased usage in solving a wide range of signal/image reconstruction problems, such as image de-blurring and super-resolution (Nehme et al., 2018), speckle imaging through random medium (Horisaki et al., 2016; Zhao et al., 2018), phase retrieval (Sinha et al., 2017), etc., thanks to their ability to approximate the inverse mapping of a complicated physical process. The use of neural networks has been explored as a viable substitution for pulse retrieval from both femtosecond

FROG traces and attosecond streaking traces (White and Chang, 2019; Zahavy et al., 2018). The flexibility of representing a wide variety of physics models means neural network-based pulse retrieval can incorporate a complete description of the streaking process, including the energy-dependent phase gating, angular distribution of photoelectrons, as well as photoelectron-laser interaction that has not been fully implemented in existing FROG-derived methods.

In most FROG-derived pulse retrieval methods, the dipole transition element, d , is assumed to be constant. This assumption does not hold for low energy (<50 eV) photoelectrons, which are subject to additional energy-dependent phase delays from Coulomb-laser coupling (Ivanov and Smirnova, 2011; Smirnova et al., 2007). This delay can be expressed as a phase term

$$d(W) = \exp(i\eta(W)) \exp(i\delta(W)), \quad (27)$$

where the energy W is expressed in atomic unit; $\eta(W) = \arg\left\{\Gamma\left(2 - i/\sqrt{2(W - I_p)}\right)\right\}$ is the phase delay from the Coulomb potential (Ivanov and Smirnova, 2011), $\Gamma[\cdot]$ representing the complex gamma function; $\delta(W) = \int_0^{W-I_p} (2W')^{3/2} (2 - \ln(W'T_{IR})) dW'$ is the phase delay from the interaction with IR dressing field (Smirnova et al., 2007), where $T_{IR} = 2\pi c/\lambda_c$ is the oscillating period of the IR field in atomic unit. The ideal streaking trace is thus modeled by

$$I(W, \tau) = \int_0^{\theta_{\max}} \left| \int_{-\infty}^{\infty} E_X(t - \tau) d(W) G(W, t, \theta) \exp(i(W + I_p)t) dt \right|^2 f(\theta) \sin(\theta) d\theta, \quad (28)$$

where the phase gate $G(W, t, \theta)$ is the same as that in Eq. (26). The angular distribution of photoemission, the energy-dependent phase delays from Coulomb-laser coupling and photoabsorption cross section of helium atom are shown in Fig. 16.

The inverse of the streaking process (Eq. 28) can be approximated by a deterministic neural network with trainable parameters ξ embedded in different layers, as shown in Fig. 14A. The input of the neural network is a discretized, two-dimensional array \mathbf{y} (Eq. 19) representing the measured counts in terms of energy W and delay τ . The X-ray and IR dressing pulses are represented by discrete parameters \mathbf{x} , which denote the real

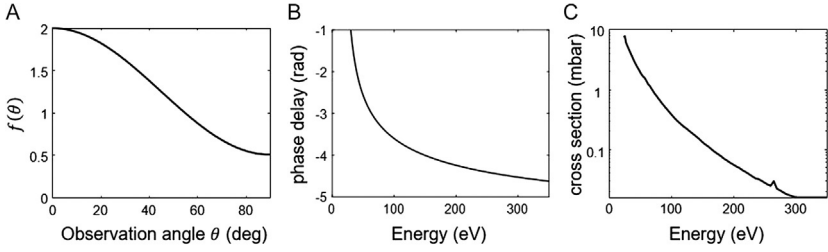


Fig. 16 Refined streaking model in learning-based pulse retrieval compared to FROG-based retrieval methods. (A) Angular distribution of induced photoelectrons $f(\theta)$. (B) Phase delay on the photoelectron as a result of Coulomb-laser coupling in 30–350 eV. (C) Photoionization cross section of helium atom in 30–350 eV.

and imaginary part of a complex field in frequency domain. The structure of the network consists of multiple convolutional layers that gradually down-sample the two-dimensional trace \mathbf{y} , followed by a fully-connected layer that connects the convolutional output to the pulse parameters \mathbf{x} (White and Chang, 2019).

The training data was generated by imposing spectral phases on the experimental X-ray and IR spectra $\tilde{E}(\epsilon) = \sqrt{S(\epsilon)} \exp i\phi(\epsilon)$, and Fourier-transform into the time domain for streak calculation. The spectral phase term was expressed as a fifth order polynomial function $\phi(\epsilon) = \sum_{i=0}^5 k_i \epsilon^i$, where ϵ is the energy in atomic unit. Notice that the carrier envelope phase (CEP) term k_0 of the XUV pulse does not affect the streaking intensity. X-ray pulses with the same phase coefficients except k_0 would yield the same ideal trace, creating ambiguities in the training dataset. The training process updates the network parameters ξ to minimize the objective function \mathcal{L}_{NN} , which is the mean square error (MSE) between the retrieved pulse parameters $\hat{\mathbf{x}}_i$ and the true parameters \mathbf{x}_i , for all the samples in the training dataset $\{(\mathbf{x}_i, \mathbf{y}_i), i = 1, \dots, N\}$

$$\mathcal{L}_{NN} = \sum_{i=1}^N \|\mathbf{x}_i - \hat{\mathbf{x}}_i\|^2 \quad (29)$$

where “ $\|\cdot\|$ ” denotes the L2 norm of the vector. Unsupervised learning (White and Chang, 2019; Zahavy et al., 2018) can also be performed by minimizing the MSE between the measured trace \mathbf{y}_i and simulated trace $\hat{\mathbf{y}}_i$ to improve the fidelity of retrieved pulse

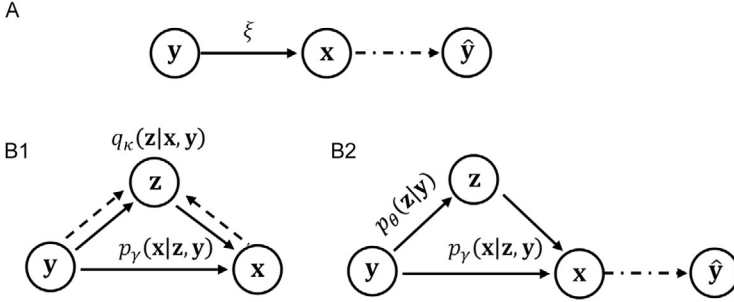


Fig. 17 Structure of neural networks used for attosecond pulse retrieval. (A) Conventional deterministic neural network that approximates the inverse of the streaking process by multiple layers with parameter ξ . (B) Conditional variational generative network (CVGN) that models the posterior of pulse parameters given an input streaking trace with a parameterized distribution $p_\gamma(x|z, y)$. Training of the network parameters γ is assisted by introducing (B1) variational inference process $q_\kappa(z|x, y)$ (dashed lines). For both networks an optional unsupervised learning (dot-dashed line) can be added for high-fidelity pulse retrieval.

$$\mathcal{L}_{NN} = \sum_{i=1}^{\mathcal{N}} |\mathbf{y}_i - \hat{\mathbf{y}}_i|^2 \quad (30)$$

where $\hat{\mathbf{y}}_i$ is calculated from the retrieved pulse parameters $\hat{\mathbf{x}}_i$ using Eq. (28). The unsupervised training is illustrated by the dot-dashed branch in Fig. 17A.

Although the aforementioned pulse retrieval networks can be trained to mimic the inversion of a complete streaking process, its output is still a deterministic X-ray and IR pulse pair, which lacks the ability to directly capture the distribution of possible pulses given a noisy streaking trace, or to resolve multiple ambiguity instances that give rise to the same ideal streaking trace. To address this demand, a probabilistic neural network framework, conditional variational generative network (CVGN, illustrated in Fig. 17B), has been introduced to model the posterior distribution of the pulse parameters \mathbf{x} , given an input streaking trace \mathbf{y} , parameterized by a latent variable \mathbf{z}

$$p_\gamma(\mathbf{x}|\mathbf{y}) = \int p_\gamma(\mathbf{x}|\mathbf{z}, \mathbf{y}) p_\gamma(\mathbf{z}|\mathbf{y}) d\mathbf{z}, \quad (31)$$

where $p_\gamma(\mathbf{z}|\mathbf{y})$ is the conditional prior distribution of \mathbf{z} , given an input streak \mathbf{y} . Both $p_\gamma(\mathbf{z}|\mathbf{y})$ and $p_\gamma(\mathbf{x}|\mathbf{z}, \mathbf{y})$ are assumed to be multivariate Gaussians with diagonal covariance, $p_\gamma(\mathbf{z}|\mathbf{y}) = \mathcal{N}(\mathbf{z}; \boldsymbol{\mu}_z^{(\gamma)}(\mathbf{y}), \text{diag}([\boldsymbol{\sigma}_z^{(\gamma)}(\mathbf{y})]^2))$, $p_\gamma(\mathbf{x}|\mathbf{z}, \mathbf{y}) = \mathcal{N}(\mathbf{x}; \boldsymbol{\mu}_x^{(\gamma)}(\mathbf{y}, \mathbf{z}), \beta \mathbf{I})$, where the mean and variance parameters $\boldsymbol{\mu}_z^{(\gamma)}(\mathbf{y})$,

$\boldsymbol{\mu}_{\mathbf{x}}^{(\gamma)}(\mathbf{y}, \mathbf{z})$ and $\boldsymbol{\sigma}_{\mathbf{z}}^{(\gamma)}(\mathbf{y})$ are implemented by neural networks with parameter γ (Zhu et al., 2019), and β is a hyper-parameter that determines the covariance of the posterior distribution.

The training process of the CVGN maximizes the joint log-likelihood $\log p_{\gamma}(\mathbf{x} | \mathbf{y}) = \sum_{i=1}^N \log p_{\gamma}(\mathbf{x}_i | \mathbf{y}_i)$ of observing the pulse parameters versus trace pairs $\{(\mathbf{x}_i, \mathbf{y}_i), i = 1, \dots, N\}$ in the dataset. Due to the intractable integral in Eq. (31), a lower bound of the log-likelihood is used as the objective function, \mathcal{L} , with the introduction of a recognition distribution $q_{\kappa}(\mathbf{z} | \mathbf{x}, \mathbf{y})$ (Kingma and Welling, 2013)

$$\begin{aligned} \log p_{\gamma}(\mathbf{x}_i | \mathbf{y}_i) &\geq -KL\left(q_{\kappa}(\mathbf{z} | \mathbf{x}_i, \mathbf{y}_i) \parallel p_{\gamma}(\mathbf{z} | \mathbf{y}_i)\right) \\ &\quad + E_{q_{\kappa}(\mathbf{z} | \mathbf{x}_i, \mathbf{y}_i)}\left(\log p_{\gamma}(\mathbf{x}_i | \mathbf{z}, \mathbf{y}_i)\right) := \mathcal{L}, \end{aligned} \quad (32)$$

where $q_{\kappa}(\mathbf{z} | \mathbf{x}_i, \mathbf{y}_i)$ captures the latent distribution conditioned on both the streaking trace and pulse parameters. If we model $q_{\kappa}(\mathbf{z} | \mathbf{x}_i, \mathbf{y}_i)$ as a multivariate Gaussian with diagonal covariance matrix $\mathcal{N}(\mathbf{z}; \boldsymbol{\mu}_{\mathbf{z}}^{(\kappa)}(\mathbf{x}, \mathbf{y}), \text{diag}([\boldsymbol{\sigma}_{\mathbf{z}}^{(\kappa)}(\mathbf{x}, \mathbf{y})]^2))$, whose mean and variance are also implemented by neural networks with parameter κ , the objective function to maximize has a closed form

$$\begin{aligned} \mathcal{L}_{CVGN} &= - \sum_{j=1}^M \left(\log \frac{\sigma_{ij}^{(\kappa)}}{\sigma_{ij}^{(\gamma)}} + \frac{(\mu_{ij}^{(\gamma)} - \mu_{ij}^{(\kappa)})^2 + \sigma_{ij}^{(\gamma)^2}}{2\sigma_{ij}^{(\phi)^2}} - \frac{1}{2} \right) \\ &\quad - \frac{1}{\beta L} \sum_{l=1}^L \left(\mathbf{x}_l - \boldsymbol{\mu}_{\mathbf{x}}^{(\gamma)}(\mathbf{z}_l, \mathbf{y}_l) \right)^2, \end{aligned} \quad (33)$$

where $\sigma_{ij}^{(\kappa)}$ denotes the j -th index of the M -element vectors $\boldsymbol{\sigma}_{\mathbf{z}}^{(\kappa)}(\mathbf{x}_i, \mathbf{y}_i)$; similar notations are applied to $\sigma_{ij}^{(\gamma)}$, $\mu_{ij}^{(\kappa)}$ and $\mu_{ij}^{(\gamma)}$. The expectation in Eq. (32) is approximated by sampling L instances of \mathbf{z} from the distribution $q_{\kappa}(\mathbf{z} | \mathbf{x}_i, \mathbf{y}_i)$ as $\{\mathbf{z}_l: l = 1, \dots, L\}$. After training the CVGN, multiple instances of pulse parameters can be retrieved from the distribution $p_{\gamma}(\mathbf{x} | \mathbf{z}, \mathbf{y})$ by sampling $\{\mathbf{z}_l: l = 1, \dots, L\}$ from the conditional prior distribution $p_{\gamma}(\mathbf{z} | \mathbf{y})$. The time- and frequency-domain XUV pulses can then be fully reconstructed from these pulse parameters.

4.3 Performance and comparisons of learning-based pulse retrieval methods

This subsection demonstrates and compares the performance of learning-based pulse retrieval methods, with focuses on resolving ambiguities in the streaking process and retrieval from noisy traces. We generated the

training dataset by creating 10,000 ideal streaking traces from randomly-sampled first to fifth order Taylor coefficients in the spectral phase. An additional 100 ideal traces were created as test dataset. The performance was evaluated by the MSE between ground truth and retrieved pulse (or reconstructed streaking traces), which were both normalized to 0–1 beforehand.

For the retrieval of ambiguity instances, we additionally generated 10 ambiguity instances of each ideal streaking trace by changing the CEP term k_0 within 0 and 2π , and trained both deterministic neural network and CVGN on this training dataset that contained ambiguity. Fig. 18

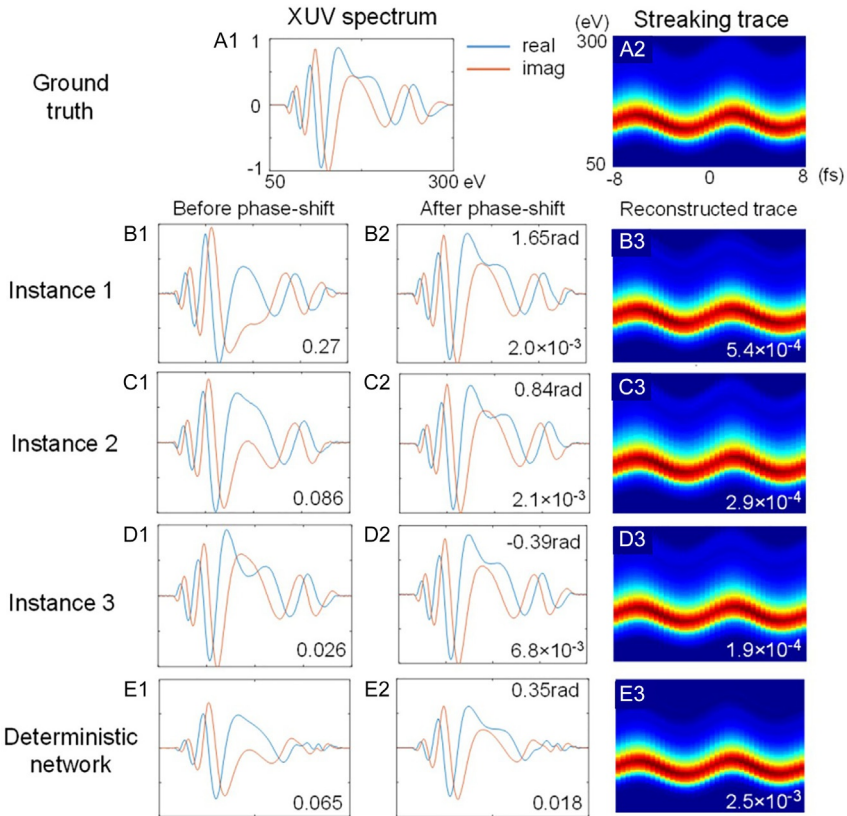


Fig. 18 Reconstructions from the ultrafast pulse retrieval experiment: (A) Ground truth of the real and imaginary part of the XUV spectrum and its simulated streak trace. The IR spectrum is not shown in the figure. (B–D) Three instances of CVGN-retrieved XUV spectrum (B1–D1), their phase-shifted variant (B2–D2), and the streaking trace (B3–D3) calculated from each instance. (E) Retrieved XUV spectrum, its phase-shifted variant and streak trace from the deterministic network.

displays the real and imaginary part of the CVGN-retrieved X-ray spectrums to highlight the differences among ambiguity instances. An ideal streaking trace (Fig. 18A2) generated from a test X-ray pulse (Fig. 18A1) was fed into the trained CVGN. Three instances of the CVGN-retrieved X-ray spectrums are shown in Fig. 18B1–D1, with MSE of 0.27, 0.086 and 0.026, respectively, compared with the ground truth in Fig. 18A. For each of the instances, we were able to shift the carrier envelop phase k_0 by the average phase difference within 100–300 eV, and match the retrieved X-ray spectrum and ground truth with good consistency. The amount of phase-shift was 1.65, 0.84 and -0.39 rad, respectively, for Fig. 18B2–D2, with MSE of 2.0×10^{-3} , 2.1×10^{-3} and 6.8×10^{-3} after the phase shift. In contrast, the deterministic network generates identical reconstructions similar to the average of all ambiguity instances. The X-ray spectrum in Fig. 18E1 cannot be phase-shifted to match the ground truth, and exhibits poor fidelity (Fig. 18E3) compared with the true streaking trace. Table 4 summarizes the average MSE of the retrievals from the test dataset. CVGN demonstrates good fidelity as it resolves the individual ambiguity instances, a capability unmatched by deterministic network. To reach similar retrieval fidelity, a deterministic network requires manually removing the ambiguity instances from the training data.

The capability of CVGN to capture the distribution of pulses given an input trace was demonstrated by noisy attosecond streaking retrieval. Based on the 10,000 ideal trace library, 10 noisy instances with 5 different Poisson average peak count $\lambda = 10, 32.5, 55, 77.5,$ and 100 were generated on each ideal streaking trace, and mixed together as the training set. The 100 ideal test trace library were populated with 10 different Poisson noise levels, λ , ranging from 5 to 100, for each trace. Both the training and test dataset did not contain ambiguity instances. Fig. 19 shows the CVGN retrieval of the noisy traces at three different Poisson noise levels $\lambda = 5, 21$ and 100. For each input noisy trace, 25 instances of the pulse parameter set, \hat{x} , were retrieved from the posterior distribution $p_\gamma(x|y, z)$, and the

Table 4 MSE of retrieved pulses and reconstructed traces using deterministic network and CVGN.

	Deterministic network	CVGN
Pulse	7.8×10^{-3}	4.1×10^{-3}
Trace	4.9×10^{-3}	7.1×10^{-4}

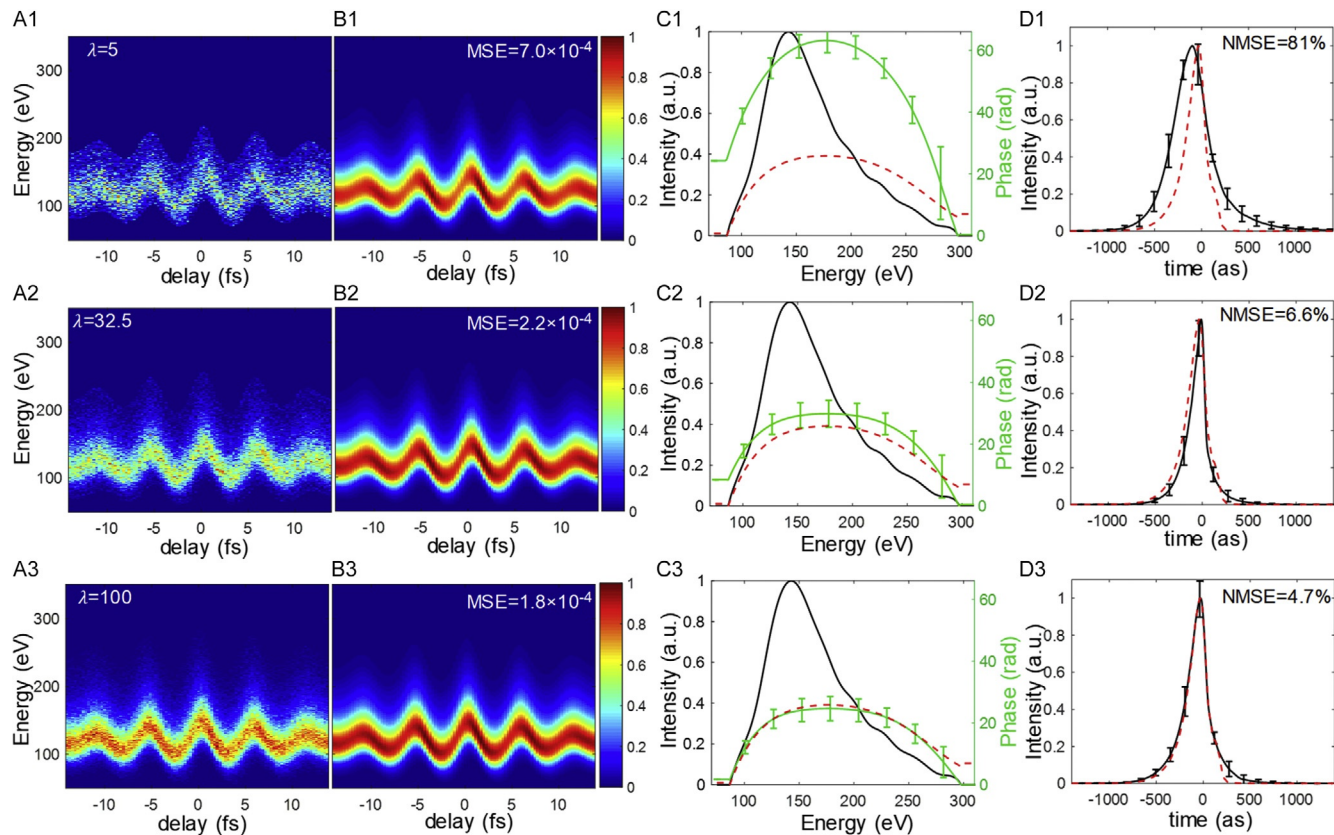


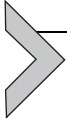
Fig. 19 Pulse retrieval from simulated noisy streaking traces. (A) Input traces with average peak counts $\lambda = 5, 21$ and 100 . (B) Reconstructed streaking trace from the retrieved pulses. The MSE indicates the error between the reconstructed streaking trace and the ground truth. (C, D) Retrieved XUV pulse in (C) frequency domain and (D) time domain. The dashed red curves on (C) and (D) indicate the ground truth of time-domain XUV intensity and spectral phase, respectively. Error bars on (C), (D) represent the variance among the retrieved XUV pulse instances. The NMSE indicates the normalized MSE of the FWHM between retrieved XUV pulse and ground truth.

frequency- and time-domain X-ray amplitude and phase were subsequently reconstructed. Streaking traces (Fig. 19B1–B3) were generated from the retrieved pulses using the physical model in Eq. (28). Error bars on Fig. 19C, D represent the variance of the 25 instances of retrieved XUV pulse.

The reconstructed streaking traces and the full-width-at-half-maximum (FWHM) of the time-domain X-ray pulse were compared with the ground truth. The MSE on pulse duration was normalized by the FWHM of the X-ray ground truth. As the average peak count, λ , increases from 5 to 32.5, the MSE of the reconstructed streaking trace decreases from 7.0×10^{-4} to 2.2×10^{-4} . The MSE of pulse duration also decreases from 81% ($\lambda=5$) down to 6.6% ($\lambda=32.5$). The results suggest a peak Poisson SNR of 6 to achieve satisfactory pulse retrieval, which could serve as a reference for future streaking experiments. It is worth noting that for low photon count (5 counts), the retrieved instances show increased bias in pulse profile, which is an indication of strong regularization (Zhu et al., 2020). This is the effect of using the training data with mixed noise level, which can be reduced by training with traces with same noise level or implementing additional mechanism to adjust the posterior distribution based on noise level.

Accurate retrieval of attosecond pulses from noisy streaking traces, which requires a complete description of the streaking process and the flexibility to model the pulse retrieval uncertainty and error, has motivated the emergence and development of learning-based pulse retrieval methods, such as deterministic neural networks and CVGN. These learning-based methods both allow complete modeling of the streaking process, including the momentum and angular distribution of the photoelectrons, as well as their interactions with the laser field photoelectron-laser interactions. Incorporating these physical processes in the streaking model eliminates the limit on the bandwidth and duration of attosecond pulses, which otherwise cannot be faithfully characterized with the assumptions in FROG-based methods. In addition, CVGN captures the distribution of possible pulses given a particular streaking trace. This unique capability helps resolve the ambiguity instances in the streaking trace, and model the uncertainty and error of the retrieved pulse from noisy experimental traces. Currently the CVGN and other neural network based pulse retrieval methods (White and Chang, 2019; Zahavy et al., 2018; Zhu et al., 2019) rely on training data generated from a measured spectrum. With better-designed network structures, the pulse parameters can be conditioned on both the streaking trace

and the measured spectrum, thus enabling the transfer of a trained network to any experimentally measured spectrum. We envision future learning-based methods to become versatile, model-based high-fidelity attosecond pulse retrieval frameworks.



5. Applications in element-specific ultrafast spectroscopy

Just as many-cycle femtosecond lasers have been used in femtochemistry to probe and study nuclear dynamics in molecules, attosecond soft X-ray sources have been used to study electron dynamics by probing K-edge and L-edge absorption edges which are particularly sensitive to changes in the molecular structure, orientation and motion. Attosecond X-ray pulses, which can be as short as tens of attoseconds, are comparable to the time scales of electron dynamics, and thus an excellent tool for time resolved spectroscopies where temporal resolution is essential for probing fast evolving dynamics.

Two typical approaches to perform time-resolved spectroscopic studies in gases (Chini et al., 2014) or condensed matter (Lépine et al., 2014; Lucchini et al., 2016; Schultze et al., 2014) is through Attosecond Transient Absorption Spectroscopy (ATAS) (Goulielmakis et al., 2010; Wang et al., 2010) or through Attosecond Photoelectron Spectroscopy (APES) (Drescher et al., 2002). Both are pump-probe techniques, and both can be used to study molecules and condensed matter. The main difference is the former records the transmission spectra of the attosecond pulse, while the latter detect the spatial-time distribution of charge fragments and electrons produced by the pump-probe interaction in the spectroscopic target.

In both pump-probe techniques, an attosecond X-ray pulse is transmitted through or reflected off a sample and is overlapped in space and time with a visible or infrared control pulse. In the case of ATAS, the transmitted attosecond spectra is recorded as a function of the relative time delay between the attosecond pulse and the control pulse. Using Ti:Sapphire driven attosecond XUV sources with spectral cutoff up to 150 eV, ATAS has been used to investigate several atoms such as krypton (Goulielmakis et al., 2010; Pabst et al., 2012), argon (Cao et al., 2016; Chew et al., 2018; Wang et al., 2010) and neon (Wang et al., 2013). ATAS has also been applied to simple molecules (Cheng et al., 2016), and condensed matter targets such as diamond (Lucchini et al., 2016) and silicon (Schultze et al., 2014).

In the case of APES, what is recorded is the spatial-time distribution of the photoelectrons emitted from the spectroscopic target. The photoelectrons travel through an electron time-of-flight tube and are imaged onto a micro-channel plate (MCP) using an appropriate electron lens. APES has been used for range of ultrafast studies, such as characterization of attosecond pulses (Drescher et al., 2001; Ferrari et al., 2010; Gaumnitz et al., 2017; Goulielmakis et al., 2008; Li et al., 2017; Sansone et al., 2006; Zhao et al., 2012), time-resolved auger decay spectroscopy for krypton (Drescher et al., 2002) and Argon (Han et al., 2019), molecular field-free alignment such as NO (Ghafur et al., 2009), N₂ (Ren et al., 2014), measuring the delay in photoemission in molecules (Cavalieri et al., 2007; Gruson et al., 2016; Klünder et al., 2011; Pazourek et al., 2015; Schultze et al., 2010), electron dynamics such as charge migration (Calegari et al., 2016a,b).

One alternative pump-probe technique is HHG spectroscopy (Corkum and Krausz, 2007; Krausz and Ivanov, 2009). The scattering of the electron wavepacket around the parent ion will thus encode structural and dynamical information of the atom or molecule in the emitting high harmonics (Lépine et al., 2014; Yun et al., 2017). This information includes Cooper minima (Higuet et al., 2011; Schoun et al., 2014; Wong et al., 2013), multi-electron dynamics (Schoun et al., 2017; Shiner et al., 2011), nonadiabatic chemical reactions (Wörner et al., 2010) and polar molecules (Kraus et al., 2012). Thus, the purpose of HHG spectroscopy (HHS) is to attempt to extract information about the molecule or atom from the emitted high harmonics; in a sense, it is an interferometer involving the electron wavepacket interfering with the parent ion. The information on the molecular orbitals can be found in the harmonic spectrum, phase and polarization, and methods were developed to measure the polarization (Lee et al., 2008; Levesque et al., 2007) and phase (Mairesse et al., 2005, 2008; Smirnova et al., 2009).

A variant of HHS is the two-dimensional HHS (Dudovich et al., 2006; Shafir et al., 2009) where through the application of a two-color field consisting of the fundamental and a weaker time-delayed orthogonally polarized second harmonic could be used to perturb the electron trajectories and to produce even-ordered harmonics and allow for the manipulation of the electron trajectories. Such a scheme could be used to probe molecules in two different axes. For example, in CO₂, odd and even high harmonics could be produced from the highest occupied molecular orbital (HOMO) and HOMO-1, respectively (Yun et al., 2015). HHS in the water window is yet to be demonstrated.

5.1 Attosecond X-ray transient absorption spectroscopy

With new infrared sources, the higher spectral cutoff has allowed for the investigation of a new range of spectroscopy targets, such as atoms, molecules and condensed matter with L and K absorption edges with the spectral bandwidth of the attosecond pulses. The X-ray absorption near-edge structures (XANES) near these absorption edges, in particular, are rich in electronic and molecular information and are highly susceptible to changes in the structure of the target. Thus far, these new infrared sources have allowed femtosecond transient absorption spectroscopy to be applied to the core excitations of carbon molecules, such as CF_4 (Pertot et al., 2017) and 1,3-cyclohexadiene (Attar et al., 2017). ATAS beyond 200 eV has been applied to inner valence excitations of titanium compounds such as TiS_2 , molecules containing sulfur such as SF_6 (Pertot et al., 2017), argon (Chew et al., 2018), and nitrogen molecules such as nitric oxide (Saito et al., 2019) (Fig. 20).

The electron dynamics observed in the various new targets through the observations of changes in the XANES spectra have been rich. In CF_4 and SF_6 , the femtosecond XANES spectra at the carbon K-edge and sulfur $L_{2,3}$ -edge were studied to monitor the reaction paths as the molecules are ionized by a strong IR field and to observe the splitting of the absorption bands as a result of symmetry breaking and the Rydberg-valence mixing due to changes in the molecule geometry. In NO, the attosecond XANES structures at the nitrogen K-edge were recorded to study the electronic, vibrational and rotational molecular dynamics at sub-picosecond to attosecond time scales as a result of the ionization of NO to NO^+ . The high degree of sensitivity of XANES spectra to the changes to the symmetry, orientation and rotational dynamics of the molecule allows experimentalists to observe molecular dynamics in “real time.”

Theoretical calculations of the ATAS spectrum require knowledge of the time-dependent dipole moment of the spectroscopy target. A qualitative description of ATAS should start with the time-dependent Schrödinger equation (TDSE) for a laser-coupled atom. Define the laser electric field \vec{F} which is linearly polarized along the z-axis as

$$\vec{F}(\vec{r}, t) = \hat{r}' F_0 \cos(-\vec{k} \cdot \vec{r} + \omega_0 t + \phi), \quad (34)$$

where F_0 is the electric field strength, \vec{k} is the wave vector, \hat{r}' is the polarization vector, \vec{r} is the position vector, and ω_0 is the angular frequency and ϕ

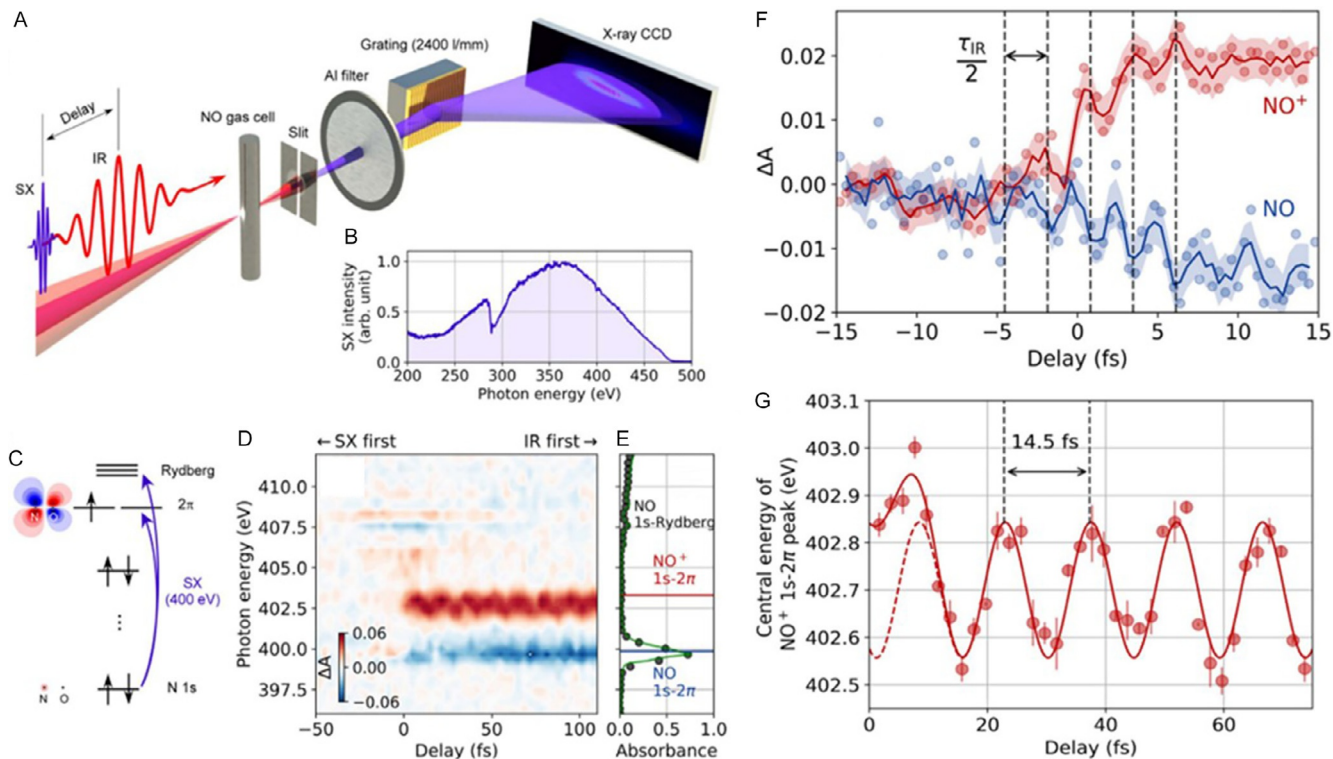


Fig. 20 Attosecond transient absorption spectroscopy at the N K-edge. (A) Experimental setup. (B) Attosecond X-ray spectrum. (C) Molecular orbitals of NO. (D) Absorption spectrogram. (E) Static absorbance of NO without the IR pump pulse. (F) Electronic response. (G) Molecular vibration. Adapted with permission from Saito, N., Sannohe, H., Ishii, N., Kanai, T., Kosugi, N., Wu, Y., Chew, A., Han, S., Chang, Z., Itatani, J., 2019. Real-time observation of electronic, vibrational, and rotational dynamics in nitric oxide with attosecond soft X-ray pulses at 400 eV. *Optica* 6, 1542. <https://doi.org/10.1364/OPTICA.6.001542> missent>/missent> The Optical Society.

is the phase. The TDSE, in atomic units and in the length gauge with the dipole approximation, is

$$i \frac{\partial \Psi(\vec{r}, t)}{\partial t} = [\hat{H}_0 + \hat{H}'(t)] |\Psi(\vec{r}, t)\rangle, \quad (35)$$

where \hat{H}_0 is the Hamiltonian for the atomic or molecular system and $\hat{H}'(t)$ is the interaction Hamiltonian defined as

$$\hat{H}'(t) = -\vec{r} \cdot \vec{F}(t, \tau) = -\vec{r} \cdot \left[\vec{F}^X(t - \tau) + \vec{F}^{IR}(t) \right], \quad (36)$$

where $\vec{F}(t, \tau)$ is the total two-color electric field, \vec{F}^X is the X-ray electric field and \vec{F}^{IR} is the IR dressing pulse electric field. τ is the time delay between the two pulses. $|\Psi(\vec{r}, t)\rangle$ is the sum of the orthogonal eigenstates of the quantum system and is in the form

$$|\Psi(\vec{r}, t)\rangle = \sum_i c_i(t) |\Psi_i(\vec{r}, t)\rangle, \quad (37)$$

where $|\Psi(\vec{r}, t)\rangle$ are the eigenstates and $c_i(t)$ is the time-dependent complex amplitude. By substituting Eq. (37) into (35) and taking the inner product, the following is obtained

$$i\dot{c}_j(t) = E_j c_j + \sum_{i \neq j} d_{ji} \left[\vec{F}^X(t - \tau) + \vec{F}^{IR}(t) \right] c_i(t), \quad (38)$$

where $d_{ji} = \langle \Psi_j | r | \Psi_i \rangle$ is the dipole moment. This equation is often solved numerically. However, for molecules and heavy atoms, obtaining their eigenstates is actually a nontrivial task. Also, ab initio approaches to the TDSE might actually be required to obtain accurate solutions. Once the values for $c_i(t)$ have been obtained, the time-dependent dipole moment can then be calculated.

The next step is to calculate the single atom response function $\tilde{S}(\omega)$ (Gaarde et al., 2011; Wu et al., 2016). The single atom response function $\tilde{S}(\omega)$ can be derived by first noting that the total energy ΔE gained by an atom is the integral over all time the rate at which energy is gained or lost by the atom, or the mean of the single atom response function,

$$\Delta E = \int_{-\infty}^{\infty} \frac{dE}{dt} dt = \int \omega \tilde{S}(\omega) d\omega, \quad (39)$$

One notes that the derivative of the energy E is also the derivative of the Hamiltonian and using Eq. (38) and

$$\frac{dE}{dt} = \frac{d}{dt} \langle \Psi | \hat{H} | \Psi \rangle = \left\langle \Psi \left| \frac{d\hat{H}}{dt} \right| \Psi \right\rangle = \langle z \rangle \frac{dF_z}{dt}, \quad (40)$$

where $\langle z \rangle = \langle \Psi(t) | z | \Psi(t) \rangle$ and the fields are assumed to be linearly polarized in the z -axis. By expanding $\langle z \rangle$, which will be written as $z(t)$ for simplicity, and $\frac{dF_z}{dt}$ in terms of their Fourier representations and rearranging the equation appropriately, Eq. (39) becomes

$$\begin{aligned} \Delta E &= \frac{1}{2\pi} \iint [z(\omega) e^{i\omega t}] [-i\omega' F_z(\omega') e^{-i\omega' t}] dt d\omega d\omega' \\ &= \int i\omega z(\omega) F_z^*(\omega) d\omega, \end{aligned} \quad (41)$$

since $z(\omega)$ is Hermitian, and the electric field is real, $z(-\omega) F_z^*(-\omega) = z^*(\omega) F_z(-\omega)$. Thus,

$$\Delta E = 2 \int_0^{\infty} \omega \text{Im} [d(\omega) F_z^*(\omega)] d\omega, \quad (42)$$

where $d(\omega) = -z(\omega)$ is the dipole spectrum. The single atom response can thus be written as

$$\tilde{S}(\omega, \tau) = 2 \text{Im} [d(\omega) F_z^*(\omega)] d\omega, \quad \omega > 0, \quad (43)$$

Finally, the ATAS spectra itself can be calculated. From the Maxwell-Bloch scalar wave equations (Santra et al., 2011), variation of the input intensity $I_{in}(\omega, \tau)$ of the electric field as a function of the time delay between the two pulses can be written as

$$\begin{aligned} I_{out}(\omega, \tau) &= I_{in}(\omega, \tau) \exp [A(\omega, \tau)] \\ &= I_{in}(\omega, \tau) \exp \left[-\frac{4\pi\omega}{c} \text{Im} \left[\frac{\tilde{P}(\omega, \tau)}{F_{in}(\omega, \tau)} \right] NL \right], \end{aligned} \quad (44)$$

This is essentially a form of the Beer-Lambert law. $A(\omega)$ is the absorbance, and $\tilde{P}(\omega, \tau)$ is the polarization of the medium. N is the atomic density and L is the length of interaction. Since $\tilde{P}(\omega, \tau)$ is essentially the dipole

moment, the absorbance $A(\omega)$ can be written as a function of the single atom response:

$$A(\omega) = -\frac{4\pi\omega}{c} \text{Im} \left[\frac{\tilde{S}(\omega, \tau)}{|F_{in}(\omega, \tau)|^2} \right] L, \quad (45)$$

The ATAS spectrum is thus calculated as such.

Electron dynamics in Argon at the $L_{2,3}$ edge using two-cycle, 3 mJ, 1.7 μm SWIR laser source (Yin et al., 2016) were studied. The aim was to study the effect of pump-probe excitation on autoionizing states; the attosecond X-ray pulse with 240–250 eV photon energy would excite electrons from the Argon $2p_{3/2}$ and $2p_{1/2}$ levels to autoionizing state. These autoionizing states will give rise to Auger electron emissions as electrons in the M level fill the holes formed by the ionized electrons and shake off another electron in the M level into the continuum. These emitted electrons constitute the Ar $L_{2,3}$ MM Auger spectrum (King et al., 1977; Werme et al., 1973).

The ATAS experimental setup is shown in Fig. 21. A strong SWIR pulse ($\sim 10^{12}$ – 10^{13} W/cm²) would induce the excited electron to tunnel into the continuum. In the recorded ATAS spectra, strong AC Stark shifts of the absorption lines and a broad spread of light induced states were observed. In addition, vertical fringes with period corresponding to twice the SWIR time period were found. The experimental results were in good agreement with theoretical calculations.

5.2 Attosecond X-ray photoelectron spectroscopy

The previous APES study of the Krypton MNN Auger spectra at 40 eV from ionization of the M-level by Drescher et al. (2002) served as a template for the study of the Argon $L_{2,3}$ MM (~ 250 eV) edges. Electron correlation, that is determined by the interaction among electrons in a multi-electron system, plays a fundamental role in a various physical processes and characterized several non-equilibrium processes. Auger decays in atoms are a representative phenomenon of such dynamics. Fig. 22 shows a mechanism of Auger decay in atoms. An incident photon or electron creates a core hole in inner-shell. An electron from a higher energy level may fall into the vacancy, resulting in a emission of energy which is form of a photon or another electron from the atom. This ejected electron is called a Auger electron. XUV pulses in water window can initiate the Auger effect by exciting the electron in the inner shell and creating core hole. XUV pulses based attosecond

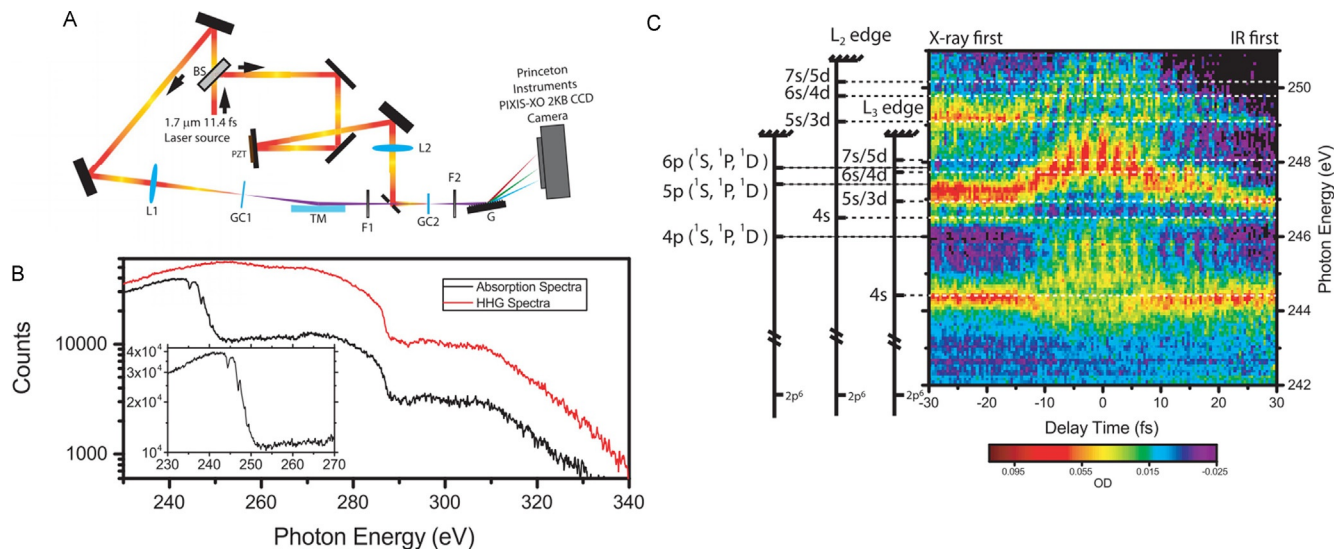


Fig. 21 Attosecond Transient Absorption of Argon. (A) The experimental setup. (B) The HHG and Argon absorption spectra as measured by the spectrometer. The insert gives an enlarged view of the Argon absorption lines at the $L_{2,3}$ edge. (C) The ATAS spectra for parallel polarized X-ray and dressing SWIR. Adapted with permission from Chew, A., Douquet, N., Cariker, C., Li, J., Lindroth, E., Ren, X., Yin, Y., Argenti, L., Hill, W.T., Chang, Z., 2018. Attosecond transient absorption spectrum of argon at the $L_{2,3}$ edge. *Phys. Rev. A* 97, 031407. <https://doi.org/10.1103/PhysRevA.97.031407>.

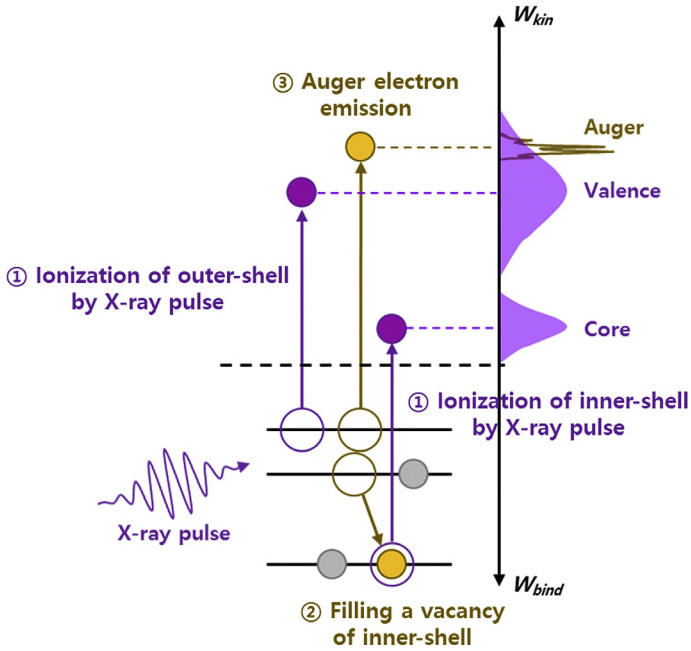


Fig. 22 Mechanism of Auger decay with X-ray pulse.

pump-probe techniques can unveil electron dynamics in the Auger effect through multiple channel in atoms or molecules.

In that experiment, the X-ray pulses used to excite electrons from the M-level had a pulse duration less than the lifetime of the core holes. The delayed near infrared probe pulse transfers momentum to the emitted Auger electrons at ~ 200 eV. The emitted Auger electrons then had an emission temporal evolution that varied with the relative delay between the pump and probe pulse where the rising front edge rises with the X-ray pulse, while the falling edge follows the decay of the core holes.

Recently, Argon Auger dynamics are unveiled by APES with < 250 eV CEP stabilized attosecond X-ray pulses in water window (Han et al., 2019). The simultaneous streaking of Auger electrons from four decay channels from the Argon L-shell with high resolution time-of-flight spectrometer with a resolution of 0.5 eV around 200 eV electron energy. Fig. 23 shows the streaking spectrogram of the evolution of the four $L_{2,3}M_{2,3}M_{2,3}$ Auger lines at different time delays between the X-ray and the IR pulses, when the L-shell electrons in Argon are excited by attosecond X-rays with > 250 eV photon energy. A positive delay corresponds to an earlier X-ray

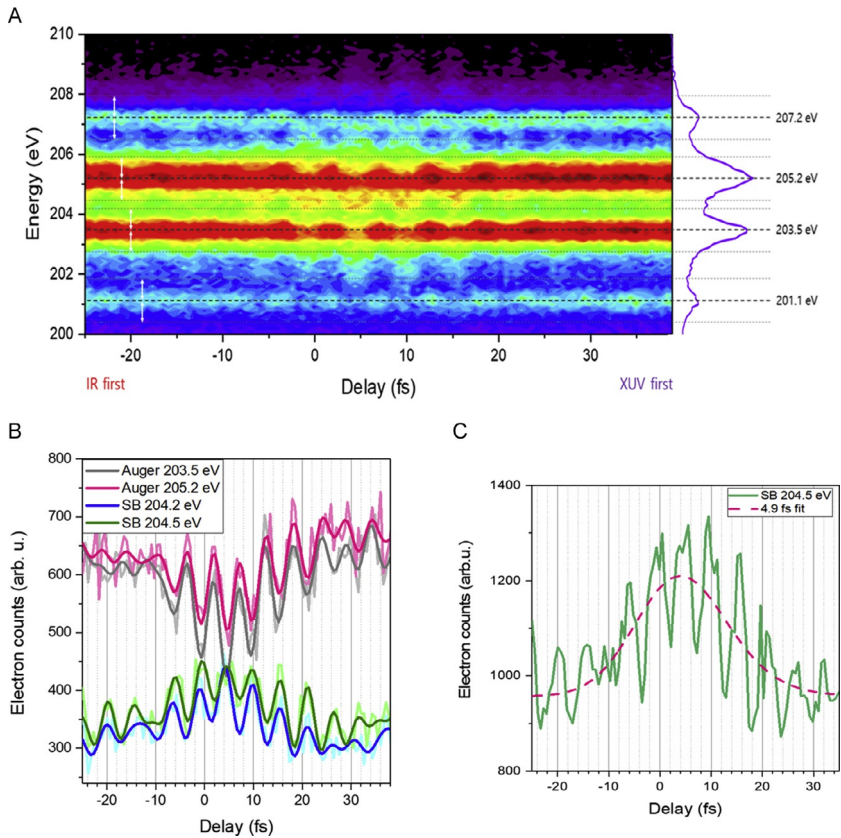


Fig. 23 Attosecond photoelectron spectroscopy on Argon Auger decay. (A) Evolution of electron spectrum following core excitation. (B) Measured electron counts of two strong Auger peaks and corresponding sideband along the delay. (C) The extracted Argon Auger decay time of 205.4 eV Auger peak from the sideband of 204.5 eV. Adapted with permission from Han, S., Xu, P., Wang, Y., Zhao, K., Chang, Z., 2019. *Stretching of argon L-shell Auger emissions with >250 eV attosecond X-ray pulses*. In: *Conference on Lasers and Electro-Optics*. OSA, Washington, D.C., p. FF3C.4. https://doi.org/10.1364/CLEO_QELS.2019.FF3C.4 missent>/missent> The Optical Society.

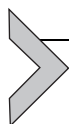
pulse arrival. The violet energy spectrum on the right side of Fig. 23A is the Auger electron spectrum induced by X-ray pulses only, which clearly shows four Auger peaks. The streaking trace contains the information about the relative time delay between Auger emissions from different channels. The Argon Auger decay time of the 205.2 eV peak is 4.9 fs and the 203.5 eV peak has a decay time of 5.6 fs (Fig. 23). These values are in good agreement with the spectroscopic measurements (Jurvansuu et al., 2001).

Future experiments in ATAS and APES would be conducted to study charge dynamics in the molecules or condensed matter with absorption edges in the water window region. One such electron dynamic which researchers would like to observe is charge migration (Cederbaum and Zobeley, 1999; Lépine et al., 2014; Remacle et al., 1999). Charge migration is an ultrafast process driven largely by electron correlation where the ionization of the molecule creates a hole that “migrates” throughout the system in the time scales of hundreds of attoseconds to a few femtoseconds as a result of the coherent superposition of states created by a pump pulse. This creation of the coherent superposition of states can be created by either a strong ionizing pump pulse, which covers a range of ionization thresholds, or the development of a large manifold of ionic states induced by electron correlation. The hole would migrate from one point in the molecule to another or oscillate along the molecular axis. Charge migration must be contrasted against charge transfer, which is a much slower process and driven by nuclear motion.

One of the first experimental observation of ultrafast charge migration was reported by Calegari et al. (2014) in the amino acid phenylalanine. In that experiment, a sub-300-as XUV pulse was used to ionize the molecule and a 4-fs time-delayed IR pulse is used as a probe pulse. The production yield of doubly charged immonium ions at each delay step was measured using a mass spectrometer and a number of few-fs oscillatory frequencies were found in the otherwise smooth curve. The oscillations were interpreted as the result of coherent charge dynamics in the cations and the theoretical calculations where the transition amplitudes of the different ionization channels were evaluated. Charge migration is still an ongoing research topic, and much theoretical studies are still being pursued (Lara-Astiaso et al., 2016; Wörner et al., 2017). Attosecond water window X-rays may allow atomic-site specific transient absorption measurement to trace the motion of the charge between C, N and O atoms in a molecule.

Another area of study would be the breakdown of the Born-Oppenheimer approximation at conical intersections. In the Born-Oppenheimer approximation, nuclear motions are regarded as sufficiently slow such that the electron wavefunction could be treated as separate from that of the nuclear wavefunction. However, at conical intersections, dynamic changes to the molecular configuration as a result of electronic and nuclear motion results in multiple potential energy surfaces being degenerate (Klessinger and Michl, 1995; Robb et al., 1995; Yarkony, 1996) and thus, a breakdown of the Born-Oppenheimer approximation. Conical intersections can be found

in photochemistry (Levine and Martínez, 2007), material science (Shu et al., 2015) and biology, but they have yet been observed with ATAS. Numerical simulations of C_2H_2 molecules have been performed by Neville et al. (2018) to study wave packet dynamics at the conical intersections when C_2H_2 molecules have been subjected to photoexcitation and probed with water window X-rays. These simulations offer the prospect that conical intersections could be studied with ATAS.



6. Summary and outlook

The recent demonstration of isolated attosecond X-rays in the water window is a breakthrough in attosecond science and technology. The high photon flux of the new generation attosecond light source enabled element specific attosecond transient absorption spectroscopy experiments at 400 eV for the first time. It is expected that high average power driving laser at 2.5 μm or even longer wavelengths will push the attosecond spectrum to the oxygen K-edge (533 eV) and beyond in the coming years.

Acknowledgments

This work was supported by United States Air Force Office of Scientific Research (AFOSR) (FA9550-15-1-0037, FA9550-16-1-0013); Army Research Office (ARO) (W911NF-14-1-0383, W911NF-19-1-0224); Defense Advanced Research Projects Agency (DARPA) (D18AC00011); National Science Foundation (1806575); Defense Threat Reduction Agency (HDTRA11910026). DSTL/EP SRC (MURI EP/N018680/1).

References

- Abel, M.J., Pfeifer, T., Nagel, P.M., Boutu, W., Bell, M.J., Steiner, C.P., Neumark, D.M., Leone, S.R., 2009. Isolated attosecond pulses from ionization gating of high-harmonic emission. *Chem. Phys.* 366, 9–14. <https://doi.org/10.1016/j.chemphys.2009.09.016>.
- Anashkina, E., Antipov, O., 2010. Electronic (population) lensing versus thermal lensing in Yb:YAG and Nd:YAG laser rods and disks. *J. Opt. Soc. Am. B* 27, 363. <https://doi.org/10.1364/josab.27.000363>.
- Attar, A.R., Bhattacharjee, A., Pemmaraju, C.D., Schnorr, K., Closser, K.D., Prendergast, D., Leone, S.R., 2017. Femtosecond X-ray spectroscopy of an electrocyclic ring-opening reaction. *Science* 356, 54–59. <https://doi.org/10.1126/science.aaj2198>.
- Baltuška, A., Fuji, T., Kobayashi, T., 2002. Controlling the carrier-envelope phase of ultra-short light pulses with optical parametric amplifiers. *Phys. Rev. Lett.* 88, 4. <https://doi.org/10.1103/PhysRevLett.88.133901>.
- Baumert, T., Brixner, T., Seyfried, V., Strehle, M., Gerber, G., 1997. Femtosecond pulse shaping by an evolutionary algorithm with feedback. *Appl. Phys. B Lasers Opt.* 65, 779–782. <https://doi.org/10.1007/s003400050346>.
- Beetar, J.E., Rivas, F., Gholam-Mirzaei, S., Liu, Y., Chini, M., 2019. Hollow-core fiber compression of a commercial Yb:KGW laser amplifier. *J. Opt. Soc. Am. B* 36, A33. <https://doi.org/10.1364/JOSAB.36.000A33>.

- Boyd, R.W., 2008. *Nonlinear Optics*. Academic Press.
- Bradley, D.J., Liddy, B., Sleat, W.E., 1971. Direct linear measurement of ultrashort light pulses with a picosecond streak camera. *Opt. Commun.* 2, 391–395. [https://doi.org/10.1016/0030-4018\(71\)90252-5](https://doi.org/10.1016/0030-4018(71)90252-5).
- Calegari, F., Ayuso, D., Trabattoni, A., Belshaw, L., De Camillis, S., Anumula, S., Frassetto, F., Poletto, L., Palacios, A., Decleva, P., Greenwood, J.B., Martín, F., Nisoli, M., 2014. Ultrafast electron dynamics in phenylalanine initiated by attosecond pulses. *Science* 346, 336–339. <https://doi.org/10.1126/science.1254061>.
- Calegari, F., Castrovilli, M., Galli, M., Månsson, E., Trabattoni, A., Ayuso, D., De Camillis, S., Frassetto, F., Poletto, L., Palacios, A., Decleva, P., Greenwood, J., Martín, F., Nisoli, M., 2016a. Ultrafast charge dynamics induced by XUV attosecond pulses in bio-relevant molecules. In: *International Conference on Ultrafast Phenomena*. OSA, Washington, D.C., UM1A.1. <https://doi.org/10.1364/UP.2016.UM1A.1>.
- Calegari, F., Trabattoni, A., Palacios, A., Ayuso, D., Castrovilli, M.C., Greenwood, J.B., Decleva, P., Martín, F., Nisoli, M., 2016b. Charge migration induced by attosecond pulses in bio-relevant molecules. *J. Phys. B Atomic Mol. Phys.* 49, 142001. <https://doi.org/10.1088/0953-4075/49/14/142001>.
- Cao, W., Warrick, E.R., Neumark, D.M., Leone, S.R., 2016. Attosecond transient absorption of argon atoms in the vacuum ultraviolet region: line energy shifts versus coherent population transfer. *New J. Phys.* 18, 013041 <https://doi.org/10.1088/1367-2630/18/1/013041>.
- Cavaliere, A.L., Müller, N., Uphues, T., Yakovlev, V.S., Baltuška, A., Horvath, B., Schmidt, B., Blümel, L., Holzwarth, R., Hendel, S., Drescher, M., Kleineberg, U., Echenique, P.M., Kienberger, R., Krausz, F., Heinzmann, U., 2007. Attosecond spectroscopy in condensed matter. *Nature* 449, 1029–1032. <https://doi.org/10.1038/nature06229>.
- Cederbaum, L.S., Zobeley, J., 1999. Ultrafast charge migration by electron correlation. *Chem. Phys. Lett.* 307, 205–210. [https://doi.org/10.1016/S0009-2614\(99\)00508-4](https://doi.org/10.1016/S0009-2614(99)00508-4).
- Cerullo, G., De Silvestri, S., 2003. Ultrafast optical parametric amplifiers. *Rev. Sci. Instrum.* 74, 1–18. <https://doi.org/10.1063/1.1523642>.
- Chang, Z., 2005. Generation of attosecond soft X-ray supercontinuum by a polarization gating. In: *Frontiers in Optics*. OSA, Washington, D.C., JTuA4. <https://doi.org/10.1364/FIO.2005.JTuA4>.
- Chang, Z., 2007. Controlling attosecond pulse generation with a double optical gating. *Phys. Rev. A: At. Mol. Opt. Phys.* 76, 1–4. <https://doi.org/10.1103/PhysRevA.76.051403>.
- Chang, Z., 2011. *Fundamentals of Attosecond Optics*. CRC Press, Taylor & Francis Group.
- Chang, Z., 2018. Attosecond chirp compensation in water window by plasma dispersion. *Opt. Express* 26, 33238. <https://doi.org/10.1364/OE.26.033238>.
- Chang, Z., 2019. Compensating chirp of attosecond X-ray pulses by a neutral hydrogen gas. In: *OSA Continuum*, vol. 2. 314. <https://doi.org/10.1364/OSAC.2.000314>.
- Chang, Z., Rundquist, A., Wang, H., Murnane, M., Kapteyn, H., 1997. Generation of coherent soft X rays at 2.7 nm using high harmonics. *Phys. Rev. Lett.* 79, 2967–2970. <https://doi.org/10.1103/PhysRevLett.79.2967>.
- Chang, Z., Corkum, P.B., Leone, S.R., 2016. Attosecond optics and technology: progress to date and future prospects [invited]. *J. Opt. Soc. Am. B* 33, 1081. <https://doi.org/10.1364/JOSAB.33.001081>.
- Cheng, Y., Chini, M., Wang, X., Gonzalez-Castrillo, A., Palacios, A., Argenti, L., Martín, F., Chang, Z., 2016. Reconstruction of an excited-state molecular wave packet with attosecond transient absorption spectroscopy. *Phys. Rev. A* 94, 023403.
- Chew, A., Douguet, N., Cariker, C., Li, J., Lindroth, E., Ren, X., Yin, Y., Argenti, L., Hill, W.T., Chang, Z., 2018. Attosecond transient absorption spectrum of argon at the $L_{2,3}$ edge. *Phys. Rev. A* 97, 031407. <https://doi.org/10.1103/PhysRevA.97.031407>.

- Chini, M., Gilbertson, S., Khan, S.D., Chang, Z., 2010. Characterizing ultrabroadband attosecond lasers. *Opt. Express* 18, 13006. <https://doi.org/10.1364/OE.18.013006>.
- Chini, M., Zhao, K., Chang, Z., 2014. The generation, characterization and applications of broadband isolated attosecond pulses. *Nat. Photonics* 8, 178–186. <https://doi.org/10.1038/nphoton.2013.362>.
- Corkum, P.B., 1993. Plasma perspective on strong field multiphoton ionization. *Phys. Rev. Lett.* 71, 1994–1997. <https://doi.org/10.1103/PhysRevLett.71.1994>.
- Corkum, P.B., Chang, Z., 2008. The attosecond revolution. *Opt. Photonics News* 19, 24. <https://doi.org/10.1364/opn.19.10.000024>.
- Corkum, P.B., Krausz, F., 2007. Attosecond science. *Nat. Phys.* 3, 381–387. <https://doi.org/10.1038/nphys620>.
- Corkum, P.B., Burnett, N.H., Ivanov, M.Y., 1994. Subfemtosecond pulses. *Opt. Lett.* 19, 1870. <https://doi.org/10.1364/ol.19.001870>.
- Cousin, S.L., Di Palo, N., Buades, B., Teichmann, S.M., Reduzzi, M., Devetta, M., Kheifets, A., Sansone, G., Biegert, J., 2017. Attosecond streaking in the water window: a new regime of attosecond pulse characterization. *Phys. Rev. X* 7, 041030. <https://doi.org/10.1103/PhysRevX.7.041030>.
- DeLoach, L.D., Page, R.H., Wilke, G.D., Payne, S.A., Krupke, W.F., 1996. Transition metal-doped zinc chalcogenides: spectroscopy and laser demonstration of a new class of gain media. *IEEE J. Quantum Electron.* 32, 885–895. <https://doi.org/10.1109/3.502365>.
- Deng, Y., Schwarz, A., Fattahi, H., Ueffing, M., Gu, X., Ossiander, M., Metzger, T., Pervak, V., Ishizuki, H., Taira, T., Kobayashi, T., Marcus, G., Krausz, F., Kienberger, R., Karpowicz, N., 2012. Carrier-envelope-phase-stable, 12 mJ, 15 cycle laser pulses at 21 μm . *Opt. Lett.* 37, 4973. <https://doi.org/10.1364/ol.37.004973>.
- DiChiara, A.D., Ghimire, S., Blaga, C.I., Sistrunk, E., Power, E.P., March, A.M., Miller, T.A., Reis, D.A., Agostini, P., DiMauro, L.F., 2012. Scaling of high-order harmonic generation in the long wavelength limit of a strong laser field. *IEEE J. Sel. Top. Quantum Electron.* 18, 419–433. <https://doi.org/10.1109/JSTQE.2011.2158391>.
- Dmitriev, V.G., Gurzadyan, G.G., Nikogosyan, D.N., 1999. Handbook of nonlinear optical crystals. In: Springer Series in Optical Sciences. Springer Berlin Heidelberg, Berlin, Heidelberg <https://doi.org/10.1007/978-3-540-46793-9>.
- Drescher, M., Hentschel, M., Kienberger, R., Tempea, G., Spielmann, C., Reider, G.A., Corkum, P.B., Krausz, F., 2001. X-ray pulses approaching the attosecond frontier. *Science* 291, 1923–1927. <https://doi.org/10.1126/science.1058561>.
- Drescher, M., Hentschel, M., Kienberger, R., Uiberacker, M., Yakovlev, V., Scrinzi, A., Westerwalbesloh, T., Kleineberg, U., Heinzmann, U., Krausz, F., 2002. Time-resolved atomic inner-shell spectroscopy. *Nature* 419, 803–807. <https://doi.org/10.1038/nature01143>.
- Dudovich, N., Smirnova, O., Levesque, J., Mairesse, Y., Ivanov, M.Y., Villeneuve, D.M., Corkum, P.B., 2006. Measuring and controlling the birth of attosecond XUV pulses. *Nat. Phys.* 2, 781–786. <https://doi.org/10.1038/nphys434>.
- Durand, M., Houard, A., Lim, K., Durécu, A., Vasseur, O., Richardson, M., 2014. Study of filamentation threshold in zinc selenide. *Opt. Express* 22, 5852. <https://doi.org/10.1364/OE.22.005852>.
- Duris, J., Li, S., Driver, T., Champenois, E.G., MacArthur, J.P., Lutman, A.A., Zhang, Z., Rosenberger, P., Aldrich, J.W., Coffee, R., Coslovich, G., Decker, F.-J., Glowia, J.M., Hartmann, G., Helml, W., Kamalov, A., Knurr, J., Krzywinski, J., Lin, M.-F., Marangos, J.P., Nantel, M., Natan, A., O’Neal, J.T., Shivaram, N., Walter, P., Wang, A.L., Welch, J.J., Wolf, T.J.A., Xu, J.Z., Kling, M.F., Bucksbaum, P.H., Zholents, A., Huang, Z., Cryan, J.P., Marinelli, A., 2020. Tunable isolated attosecond X-ray pulses with gigawatt peak power from a free-electron laser. *Nat. Photonics* 14, 30–36. <https://doi.org/10.1038/s41566-019-0549-5>.

- Fabris, D., Witting, T., Okell, W.a., Walke, D.J., Matia-Hernando, P., Henkel, J., Barillot, T.R., Lein, M., Marangos, J.P., Tisch, J.W.G., 2015. Synchronized pulses generated at 20 eV and 90 eV for attosecond pump–probe experiments. *Nat. Photonics* 9, 383–387. <https://doi.org/10.1038/nphoton.2015.77>.
- Ferrari, F., Calegari, F., Lucchini, M., Vozzi, C., Stagira, S., Sansone, G., Nisoli, M., 2010. High-energy isolated attosecond pulses generated by above-saturation few-cycle fields. *Nat. Photonics* 4, 875–879. <https://doi.org/10.1038/nphoton.2010.250>.
- Ferray, M., L’Huillier, A., Li, X.F., Lompre, L.A., Mainfray, G., Manus, C., 1988. Multiple-harmonic conversion of 1064 nm radiation in rare gases. *J. Phys. B Atomic Mol. Phys.* 21, L31–L35. <https://doi.org/10.1088/0953-4075/21/3/001>.
- Fuji, T., Apolonski, A., Krausz, F., 2004. Self-stabilization of carrier-envelope offset phase by use of difference-frequency generation. *Opt. Lett.* 29, 632. <https://doi.org/10.1364/ol.29.000632>.
- Fuji, T., Ishii, N., Teisset, C.Y., Gu, X., Metzger, T., Baltuska, A., Forget, N., Kaplan, D., Galvanauskas, A., Krausz, F., 2006. Parametric amplification of few-cycle carrier-envelope phase-stable pulses at 21 μm . *Opt. Lett.* 31, 1103. <https://doi.org/10.1364/ol.31.001103>.
- Gaarde, M.B., Buth, C., Tate, J.L., Schafer, K.J., 2011. Transient absorption and reshaping of ultrafast XUV light by laser-dressed helium. *Phys. Rev. A* 83, 013419. <https://doi.org/10.1103/PhysRevA.83.013419>.
- Gaumnitz, T., Jain, A., Pertot, Y., Huppert, M., Jordan, I., Ardana-Lamas, F., Wörner, H.J., 2017. Streaking of 43-attosecond soft-X-ray pulses generated by a passively CEP-stable mid-infrared driver. *Opt. Express* 25, 27506–27518. <https://doi.org/10.1364/OE.25.027506>.
- Gaumnitz, T., Jain, A., Wörner, H.J., 2018. Complete reconstruction of ultra-broadband isolated attosecond pulses including partial averaging over the angular distribution. *Opt. Express* 26, 14719. <https://doi.org/10.1364/oe.26.014719>.
- Geissler, M., Tempea, G., Brabec, T., 2000. Phase-matched high-order harmonic generation in the nonadiabatic limit. *Phys. Rev. A: At. Mol. Opt. Phys.* 62, 8. <https://doi.org/10.1103/PhysRevA.62.033817>.
- Ghafur, O., Rouzée, A., Gijbbersen, A., Siu, W.K., Stolte, S., Vrakking, M.J.J., 2009. Impulsive orientation and alignment of quantum-state-selected NO molecules. *Nat. Phys.* 5, 289–293. <https://doi.org/10.1038/nphys1225>.
- Goulielmakis, E., Schultze, M., Hofstetter, M., Yakovlev, V.S., Gagnon, J., Uiberacker, M., Aquila, A.L., Gullikson, E.M., Attwood, D.T., Kienberger, R., Krausz, F., Kleineberg, U., 2008. Single-cycle nonlinear optics. *Science* 320, 1614–1617. <https://doi.org/10.1126/science.1157846>.
- Goulielmakis, E., Loh, Z.-H., Wirth, A., Santra, R., Rohringer, N., Yakovlev, V.S., Zherebtsov, S., Pfeifer, T., Azzeer, A.M., Kling, M.F., Leone, S.R., Krausz, F., 2010. Real-time observation of valence electron motion. *Nature* 466, 739–743. <https://doi.org/10.1038/nature09212>.
- Gruson, V., Barreau, L., Jiménez-Galan, Á., Risoud, F., Caillat, J., Maquet, A., Carré, B., Lepetit, F., Hergott, J.-F., Ruchon, T., Argenti, L., Taïeb, R., Martín, F., Salières, P., 2016. Attosecond dynamics through a Fano resonance: monitoring the birth of a photoelectron. *Science* 354, 734–738. <https://doi.org/10.1126/science.aah5188>.
- Guggenmos, A., Rauhut, R., Hofstetter, M., Hertrich, S., Nickel, B., Schmidt, J., Gullikson, E.M., Seibald, M., Schnick, W., Kleineberg, U., 2013. Aperiodic CrSc multilayer mirrors for attosecond water window pulses. *Opt. Express* 21, 21728. <https://doi.org/10.1364/oe.21.021728>.
- Han, S., Xu, P., Wang, Y., Zhao, K., Chang, Z., 2019. Streaking of Argon L-shell Auger emissions with >250 eV attosecond X-ray pulses. In: *Conference on Lasers and Electro-Optics*. OSA, Washington, D.C., FF3C.4. https://doi.org/10.1364/CLEO_QELS.2019.FF3C.4.

- Haworth, C.A., Chipperfield, L.E., Robinson, J.S., Knight, P.L., Marangos, J.P., Tisch, J.W.G., 2007. Half-cycle cutoffs in harmonic spectra and robust carrier-envelope phase retrieval. *Nat. Phys.* 3, 52–57. <https://doi.org/10.1038/nphys463>.
- Hentschel, M., Kienberger, R., Spielmann, C., Reider, G.A., Milosevic, N., Brabec, T., Corkum, P., Heinzmann, U., Drescher, M., Krausz, F., 2001. Attosecond metrology. *Nature* 414, 509–513. <https://doi.org/10.1038/35107000>.
- Higuet, J., Ruf, H., Thiré, N., Cireasa, R., Constant, E., Cormier, E., Descamps, D., Mével, E., Petit, S., Pons, B., Mairesse, Y., Fabre, B., 2011. High-order harmonic spectroscopy of the Cooper minimum in argon: experimental and theoretical study. *Phys. Rev. A* 83, 053401. <https://doi.org/10.1103/PhysRevA.83.053401>.
- Hömmrich, U., Wu, X., Davis, V.R., Trivedi, S.B., Graszka, K., Chen, R.J., Kutcher, S., 1997. Demonstration of room-temperature laser action at 25 μm from $\text{Cr}^{2+}:\text{Cd}_2\text{O}_8$. *Opt. Lett.* 22, 1180. <https://doi.org/10.1364/ol.22.001180>.
- Horisaki, R., Takagi, R., Tanida, J., 2016. Learning-based imaging through scattering media. *Opt. Express* 24, 13738. <https://doi.org/10.1364/oe.24.013738>.
- Innerhofer, E., Südmeyer, T., Brunner, F., Häring, R., Aschwanden, A., Paschotta, R., Hönninger, C., Kumkar, M., Keller, U., 2003. 60-W average power in 810-fs pulses from a thin-disk Yb:YAG laser. *Opt. Lett.* 28, 367. <https://doi.org/10.1364/ol.28.000367>.
- Ishii, N., Kaneshima, K., Kitano, K., Kanai, T., Watanabe, S., Itatani, J., 2012. Sub-two-cycle, carrier-envelope phase-stable, intense optical pulses at 16 μm from a BiB_3O_6 optical parametric chirped-pulse amplifier. *Opt. Lett.* 37, 4182. <https://doi.org/10.1364/ol.37.004182>.
- Ishii, N., Kaneshima, K., Kitano, K., Kanai, T., Watanabe, S., Itatani, J., 2014. Carrier-envelope phase-dependent high harmonic generation in the water window using few-cycle infrared pulses. *Nat. Commun.* 5, 3331. <https://doi.org/10.1038/ncomms4331>.
- Itatani, J., Quéré, F., Yudin, G.L., Ivanov, M.Y., Krausz, F., Corkum, P.B., 2002. Attosecond streak camera. *Phys. Rev. Lett.* 88, 4. <https://doi.org/10.1103/PhysRevLett.88.173903>.
- Ivanov, M., Smirnova, O., 2011. How accurate is the attosecond streak camera? *Phys. Rev. Lett.* 107, 1–5. <https://doi.org/10.1103/PhysRevLett.107.213605>.
- Jin, C., Chen, M.-C., Sun, H.-W., Lin, C.D., 2018. Extension of water-window harmonic cutoff by laser defocusing-assisted phase matching. *Opt. Lett.* 43, 4433. <https://doi.org/10.1364/ol.43.004433>.
- Johnson, A.S., Miseikis, L., Wood, D.A., Austin, D.R., Brahms, C., Jarosch, S., Strüber, C.S., Ye, P., Marangos, J.P., 2016. Measurement of sulfur L2,3 and carbon K edge XANES in a polythiophene film using a high harmonic supercontinuum. *Struct. Dyn.* 3, 062603. <https://doi.org/10.1063/1.4964821>.
- Johnson, A.S., Austin, D.R., Wood, D.A., Brahms, C., Gregory, A., Holzner, K.B., Jarosch, S., Larsen, E.W., Parker, S., Strüber, C.S., Ye, P., Tisch, J.W.G., Marangos, J.P., 2018. High-flux soft X-ray harmonic generation from ionization-shaped few-cycle laser pulses. *Sci. Adv.* 4, eaar3761. <https://doi.org/10.1126/sciadv.aar3761>.
- Jurvansuu, M., Kivimäki, A., Aksela, S., 2001. Inherent lifetime widths of Ar 2p-1, Kr 3d-1, Xe 3d-1, and Xe 4d-1 states. *Phys. Rev. A* 64, 012502. <https://doi.org/10.1103/PhysRevA.64.012502>.
- Kane, D.J., 1999. Recent progress toward real-time measurement of ultrashort laser pulses. *IEEE J. Quantum Electron.* 35, 421–431. <https://doi.org/10.1109/3.753647>.
- Kane, D.J., Rodriguez, G., Taylor, A.J., Clement, T.S., 1997. Simultaneous measurement of two ultrashort laser pulses from a single spectrogram in a single shot. *J. Opt. Soc. Am. B* 14, 935. <https://doi.org/10.1364/JOSAB.14.000935>.

- Keathley, P.D., Bhardwaj, S., Moses, J., Laurent, G., Kärtner, F.X., 2016. Volkov transform generalized projection algorithm for attosecond pulse characterization. *New J. Phys.* 18, 073009. <https://doi.org/10.1088/1367-2630/18/7/073009>.
- Kennedy, D.J., Manson, S.T., 1972. Photoionization of the noble gases: cross sections and angular distributions. *Phys. Rev. A* 5, 227–247. <https://doi.org/10.1103/PhysRevA.5.227>.
- King, G.C., Tronc, M., Read, F.H., Bradford, R.C., 1977. An investigation of the structure near the L_{2,3}edges of argon, the M_{4,5}edges of krypton and the N_{4,5}edges of xenon, using electron impact with high resolution. *J. Phys. B: At. Mol. Phys.* 10, 2479–2495. <https://doi.org/10.1088/0022-3700/10/12/026>.
- Kingma, D.P., Welling, M., 2013. Auto-encoding variational bayes. *arXiv1312.6114*.
- Klessinger, M., Michl, J., 1995. *Excited States and Photochemistry of Organic Molecules*. VCH.
- Klünder, K., Dahlström, J.M., Gisselbrecht, M., Fordell, T., Swoboda, M., Guénot, D., Johnsson, P., Caillat, J., Mauritsson, J., Maquet, A., Taïeb, R., L’Huillier, A., 2011. Probing single-photon ionization on the attosecond time scale. *Phys. Rev. Lett.* 106, 143002. <https://doi.org/10.1103/PhysRevLett.106.143002>.
- Koerner, J., Vorholt, C., Liebetrau, H., Kahle, M., Kloepfel, D., Seifert, R., Hein, J., Kaluza, M.C., 2012. Measurement of temperature-dependent absorption and emission spectra of Yb:YAG, Yb:LuAG, and Yb:CaF₂ between 20 °C and 200 °C and predictions on their influence on laser performance. *J. Opt. Soc. Am. B* 29, 2493. <https://doi.org/10.1364/josab.29.002493>.
- Kraus, P.M., Rupenyan, A., Wörner, H.J., 2012. High-harmonic spectroscopy of oriented OCS molecules: emission of even and odd harmonics. *Phys. Rev. Lett.* 109, 233903. <https://doi.org/10.1103/PhysRevLett.109.233903>.
- Krausz, F., Ivanov, M., 2009. Attosecond physics. *Rev. Mod. Phys.* 81, 163–234. <https://doi.org/10.1103/RevModPhys.81.163>.
- Lara-Astiaso, M., Ayuso, D., Tavernelli, I., Decleva, P., Palacios, A., Martín, F., 2016. Decoherence, control and attosecond probing of XUV-induced charge migration in biomolecules. A theoretical outlook. In: *Faraday Discussions*. Royal Society of Chemistry, pp. 41–59. <https://doi.org/10.1039/c6fd00074f>.
- Le Blanc, C., Curley, P., Salin, F., 1996. Gain-narrowing and gain-shifting of ultra-short pulses in Ti: sapphire amplifiers. *Opt. Commun.* 131, 391–398. [https://doi.org/10.1016/0030-4018\(96\)00262-3](https://doi.org/10.1016/0030-4018(96)00262-3).
- Lee, G.H., Kim, I.J., Park, S.B., Kim, T.K., Nam, C.H., 2008. Measurement of the polarization of high-order harmonics from aligned N₂ molecules by spatial interferometry. *Opt. Lett.* 33, 2083. <https://doi.org/10.1364/ol.33.002083>.
- Lenzner, M., Spielmann, C., Wintner, E., Krausz, F., Schmidt, A.J., 1995. Sub-20-fs, kilohertz-repetition-rate Ti:sapphire amplifier. *Opt. Lett.* 20, 1397. <https://doi.org/10.1364/ol.20.001397>.
- Lépine, F., Ivanov, M.Y., Vrakking, M.J.J., 2014. Attosecond molecular dynamics: fact or fiction? *Nat. Photonics* 8, 195–204. <https://doi.org/10.1038/nphoton.2014.25>.
- Levesque, J., Mairesse, Y., Dudovich, N., Pépin, H., Kieffer, J.-C., Corkum, P.B., Villeneuve, D.M., 2007. Polarization state of high-order harmonic emission from aligned molecules. *Phys. Rev. Lett.* 99, 243001. <https://doi.org/10.1103/PhysRevLett.99.243001>.
- Levine, B.G., Martínez, T.J., 2007. Isomerization through conical intersections. *Annu. Rev. Phys. Chem.* 58, 613–634. <https://doi.org/10.1146/annurev.physchem.57.032905.104612>.
- Lewenstein, M., Balcou, P., Ivanov, M.Y., L’Huillier, A., Corkum, P.B., 1994. Theory of high-harmonic generation by low-frequency laser fields. *Phys. Rev. A* 49, 2117–2132. <https://doi.org/10.1103/PhysRevA.49.2117>.

- Li, J., 2018. Generation and Characterization of Isolated Attosecond Pulse in the Soft X-ray Regime. University of Central Florida.
- Li, C., Moon, E., Chang, Z., 2006. Carrier-envelope phase shift caused by variation of grating separation. *Opt. Lett.* 31, 3113. <https://doi.org/10.1364/ol.31.003113>.
- Li, J., Ren, X., Yin, Y., Cheng, Y., Cunningham, E., Wu, Y., Chang, Z., 2016. Polarization gating of high harmonic generation in the water window. *Appl. Phys. Lett.* 108, 231102. <https://doi.org/10.1063/1.4953402>.
- Li, J., Ren, X., Yin, Y., Zhao, K., Chew, A., Cheng, Y., Cunningham, E., Wang, Y., Hu, S., Wu, Y., Chini, M., Chang, Z., 2017. 53-attosecond X-ray pulses reach the carbon K-edge. *Nat. Commun.* 8, 186. <https://doi.org/10.1038/s41467-017-00321-0>.
- Li, J., Chew, A., Hu, S., White, J., Ren, X., Han, S., Yin, Y., Wang, Y., Wu, Y., Chang, Z., 2019. Double optical gating for generating high flux isolated attosecond pulses in the soft X-ray regime. *Opt. Express* 27, 30280. <https://doi.org/10.1364/oe.27.030280>.
- Lorek, E., Larsen, E.W., Heyl, C.M., Carlström, S., Paleček, D., Zigmantas, D., Mauritsson, J., 2014. High-order harmonic generation using a high-repetition-rate turn-key laser. *Rev. Sci. Instrum.* 85, 123106. <https://doi.org/10.1063/1.4902819>.
- Louisy, M., Arnold, C.L., Miranda, M., Larsen, E.W., Bengtsson, S.N., Kroon, D., Kotur, M., Guénot, D., Rading, L., Rudawski, P., Brizuela, F., Campi, F., Kim, B., Jarnac, A., Houard, A., Mauritsson, J., Johnsson, P., L'Huillier, A., Heyl, C.M., 2015. Gating attosecond pulses in a noncollinear geometry. *Optica* 2, 563. <https://doi.org/10.1364/OPTICA.2.000563>.
- Lucchini, M., Sato, S.A., Ludwig, A., Herrmann, J., Volkov, M., Kasmi, L., Shinohara, Y., Yabana, K., Gallmann, L., Keller, U., 2016. Attosecond dynamical Franz-Keldysh effect in polycrystalline diamond-SI. *Science* 353, 916–919. <https://doi.org/10.1126/science.aag1268>.
- Mairesse, Y., Quéré, F., 2005. Frequency-resolved optical gating for complete reconstruction of attosecond bursts. *Phys. Rev. A: At. Mol. Opt. Phys.* 71, 1–4. <https://doi.org/10.1103/PhysRevA.71.011401>.
- Mairesse, Y., Gobert, O., Breger, P., Merdji, H., Meynadier, P., Monchicourt, P., Perdrix, M., Salières, P., Carré, B., 2005. High harmonic XUV spectral phase interferometry for direct electric-field reconstruction. *Phys. Rev. Lett.* 94, 173903. <https://doi.org/10.1103/PhysRevLett.94.173903>.
- Mairesse, Y., Zeidler, D., Dudovich, N., Spanner, M., Levesque, J., Villeneuve, D.M., Corkum, P.B., 2008. High-order harmonic transient grating spectroscopy in a molecular jet. *Phys. Rev. Lett.* 100, 143903. <https://doi.org/10.1103/PhysRevLett.100.143903>.
- Major, A., Yoshino, F., Nikolakakos, I., Aitchison, J.S., Smith, P.W.E., 2004. Dispersion of the nonlinear refractive index in sapphire. *Opt. Lett.* 29, 602. <https://doi.org/10.1364/ol.29.000602>.
- Maksimenka, R., Nuernberger, P., Lee, K.F., Bonvalet, A., Milkiewicz, J., Barta, C., Klima, M., Oksenhendler, T., Tournois, P., Kaplan, D., Joffe, M., 2010. Direct mid-infrared femtosecond pulse shaping with a calomel acousto-optic programmable dispersive filter. *Opt. Lett.* 35, 3565. <https://doi.org/10.1364/ol.35.003565>.
- Mashiko, H., Nakamura, C.M., Li, C., Moon, E., Wang, H., Tackett, J., Chang, Z., 2007. Carrier-envelope phase stabilized 5.6fs, 1.2mJ pulses. *Appl. Phys. Lett.* 90, 161114. <https://doi.org/10.1063/1.2724919>.
- Mashiko, H., Gilbertson, S., Li, C., Khan, S.D., Shakya, M.M., Moon, E., Chang, Z., 2008. Double optical gating of high-order harmonic generation with carrier-envelope phase stabilized lasers. *Phys. Rev. Lett.* 100, 1–4. <https://doi.org/10.1103/PhysRevLett.100.103906>.
- Mashiko, H., Gilbertson, S., Chini, M., Feng, X., Yun, C., Wang, H., Khan, S.D., Chen, S., Chang, Z., 2009. Extreme ultraviolet supercontinua supporting pulse durations of less than one atomic unit of time. *Opt. Lett.* 34, 3337. <https://doi.org/10.1364/ol.34.003337>.

- Mauritsson, J., Johnsson, P., Gustafsson, E., L'Huillier, A., Schafer, K.J., Gaarde, M.B., 2006. Attosecond pulse trains generated using two color laser fields. *Phys. Rev. Lett.* 97, 1–4. <https://doi.org/10.1103/PhysRevLett.97.013001>.
- McPherson, A., Gibson, G., Jara, H., Johann, U., Luk, T.S., McIntyre, I.A., Boyer, K., Rhodes, C.K., 1987. Studies of multiphoton production of vacuum-ultraviolet radiation in the rare gases. *J. Opt. Soc. Am. B* 4, 595. <https://doi.org/10.1364/JOSAB.4.000595>.
- Nayak, A., Dumergue, M., Kühn, S., Mondal, S., Csizmadia, T., Harshitha, N.G., Füle, M., Upadhyay Kahaly, M., Farkas, B., Major, B., Szaszó-Bogár, V., Földi, P., Majorosi, S., Tsatrafyllis, N., Skantzakis, E., Neoričić, L., Shirozhan, M., Vampa, G., Varjú, K., Tzallas, P., Sansone, G., Charalambidis, D., Kahaly, S., 2019. Saddle point approaches in strong field physics and generation of attosecond pulses. *Phys. Rep.* 833, 1–52. <https://doi.org/10.1016/j.physrep.2019.10.002>.
- Nehme, E., Weiss, L.E., Michaeli, T., Shechtman, Y., 2018. Deep-STORM: super-resolution single-molecule microscopy by deep learning. *Optica* 5, 458. <https://doi.org/10.1364/OPTICA.5.000458>.
- Neville, S.P., Chergui, M., Stolow, A., Schuurman, M.S., 2018. Ultrafast X-ray spectroscopy of conical intersections. *Phys. Rev. Lett.* 120, 243001. <https://doi.org/10.1103/PhysRevLett.120.243001>.
- Pabst, S., Sytcheva, A., Moulet, A., Wirth, A., Goulielmakis, E., Santra, R., 2012. Theory of attosecond transient-absorption spectroscopy of krypton for overlapping pump and probe pulses. *Phys. Rev. A* 86, 063411. <https://doi.org/10.1103/PhysRevA.86.063411>.
- Page, R.H., Skidmore, J.A., Schaffers, K.I., Beach, R.J., Payne, S.A., Krupke, W.F., 1997. Demonstrations of diode-pumped and grating-tuned ZnSe:Cr²⁺ lasers. In: *Advanced Solid State Lasers*. OSA, Washington, D.C., p. LS6. <https://doi.org/10.1364/ASSL.1997.LS6>.
- Papadogiannis, N.A., Kalpouzos, C., Goulielmakis, E., Nersisyan, G., Charalambidis, D., Augé, F., Weihe, F., Balcou, P., 2001. Kiloherz extreme-ultraviolet light source based on femtosecond high-order harmonic generation from noble gases. *Appl. Phys. B Lasers Opt.* 73, 687–692. <https://doi.org/10.1007/s003400100734>.
- Paul, P.M., 2001. Observation of a train of attosecond pulses from high harmonic generation. *Science* 292, 1689–1692. <https://doi.org/10.1126/science.1059413>.
- Pazourek, R., Nagele, S., Burgdörfer, J., 2015. Attosecond chronoscopy of photoemission. *Rev. Mod. Phys.* 87, 765–802. <https://doi.org/10.1103/RevModPhys.87.765>.
- Pertot, Y., Schmidt, C., Matthews, M., Chauvet, A., Huppert, M., Svoboda, V., Von Conta, A., Tehlar, A., Baykusheva, D., Wolf, J.P., Wörner, H.J., 2017. Time-resolved X-ray absorption spectroscopy with a water window high-harmonic source. *Science* 355, 264–267. <https://doi.org/10.1126/science.aah6114>.
- Petrov, V., Ghotbi, M., Kokabee, O., Esteban-Martin, A., Noack, F., Gaydardzhiev, A., Nikolov, I., Tzankov, P., Buchvarov, I., Miyata, K., Majchrowski, A., Kityk, I.V., Rotermund, F., Michalski, E., Ebrahim-Zadeh, M., 2010. Femtosecond nonlinear frequency conversion based on BiB₃O₆. *Laser Photonics Rev.* 4, 53–98. <https://doi.org/10.1002/lpor.200810075>.
- Poletto, L., Frassetto, F., Villoresi, P., 2008. Design of an extreme-ultraviolet attosecond compressor. *J. Opt. Soc. Am. B* 25, B133. <https://doi.org/10.1364/josab.25.00b133>.
- Popmintchev, T., Chen, M.C., Bahabad, A., Gerrity, M., Sidorenko, P., Cohen, O., Christov, I.P., Murnane, M.M., Kapteyn, H.C., 2009. Phase matching of high harmonic generation in the soft and hard X-ray regions of the spectrum. *Proc. Natl. Acad. Sci. U. S. A.* 106, 10516–10521. <https://doi.org/10.1073/pnas.0903748106>.
- Pupeikis, J., Chevreuril, P.-A., Bigler, N., Gallmann, L., Phillips, C.R., Keller, U., 2019. Water window soft X-ray source enabled by 25-W few-cycle mid-IR OPCPA at 100 kHz. *arXiv* 1910.03236.

- Remacle, F., Levine, R.D., Schlag, E.W., Weinkauf, R., 1999. Electronic control of site selective reactivity: a model combining charge migration and dissociation. *J. Phys. Chem. A* 103, 10149–10158. <https://doi.org/10.1021/jp991853k>.
- Ren, X., Makhija, V., Li, H., Kling, M.F., Kumarappan, V., 2014. Alignment-assisted field-free orientation of rotationally cold CO molecules. *Phys. Rev. A* 90, 013419. <https://doi.org/10.1103/PhysRevA.90.013419>.
- Ren, X., Li, J., Yin, Y., Zhao, K., Chew, A., Wang, Y., Hu, S., Cheng, Y., Cunningham, E., Wu, Y., Chini, M., Chang, Z., 2018a. Attosecond light sources in the water window. *J. Opt.* 20, 023001. <https://doi.org/10.1088/2040-8986/aaa394>.
- Ren, X., Mach, L.H., Yin, Y., Wang, Y., Chang, Z., 2018b. Generation of 1 kHz, 23 mJ, 88 fs, 25 μm pulses from a Cr 2+:ZnSe chirped pulse amplifier. *Opt. Lett.* 43, 3381. <https://doi.org/10.1364/OL.43.003381>.
- Robb, M.A., Bernardi, F., Olivucci, M., 1995. Conical intersections as a mechanistic feature of organic photochemistry. *Pure Appl. Chem.* 67, 783–789. <https://doi.org/10.1351/pac199567050783>.
- Rundquist, A., Rundquist, A., Durfee, C.G., Chang, Z., Herne, C., Backus, b., Murnane, M.M., Kapteyn, H.C., 1998. Phase-matched generation of coherent soft X-rays. *Science* 280, 1412–1415. <https://doi.org/10.1126/science.280.5368.1412>.
- Saito, N., Sannohe, H., Ishii, N., Kanai, T., Kosugi, N., Wu, Y., Chew, A., Han, S., Chang, Z., Itatani, J., 2019. Real-time observation of electronic, vibrational, and rotational dynamics in nitric oxide with attosecond soft X-ray pulses at 400 eV. *Optica* 6, 1542. <https://doi.org/10.1364/OPTICA.6.001542>.
- Salières, P., L’Huillier, A., Lewenstein, M., 1995. Coherence control of high-order harmonics. *Phys. Rev. Lett.* 74, 3776–3779. <https://doi.org/10.1103/PhysRevLett.74.3776>.
- Sansone, G., Benedetti, E., Calegari, F., Vozzi, C., Avaldi, L., Flammini, R., Poletto, L., Villoresi, P., Altucci, C., Velotta, R., Stagira, S., De Silvestri, S., Nisoli, M., 2006. Isolated single-cycle attosecond pulses. *Science* 314, 443–446. <https://doi.org/10.1126/science.1132838>.
- Sansone, G., Ferrari, F., Vozzi, C., Calegari, F., Stagira, S., Nisoli, M., 2009. Towards atomic unit pulse duration by polarization-controlled few-cycle pulses. *J. Phys. B Atomic Mol. Phys.* 42, 134005. <https://doi.org/10.1088/0953-4075/42/13/134005>.
- Santra, R., Yakovlev, V.S., Pfeifer, T., Loh, Z.-H., 2011. Theory of attosecond transient absorption spectroscopy of strong-field-generated ions. *Phys. Rev. A* 83, 033405. <https://doi.org/10.1103/PhysRevA.83.033405>.
- Schafer, K.J., Yang, B., DiMauro, L.F., Kulander, K.C., 1993. Above threshold ionization beyond the high harmonic cutoff. *Phys. Rev. Lett.* 70, 1599–1602. <https://doi.org/10.1103/PhysRevLett.70.1599>.
- Schötz, J., Förg, B., Schweinberger, W., Lontos, I., Masood, H.A., Kamal, A.M., Jakubeit, C., Kling, N.G., Paasch-Colberg, T., Högner, M., Pupeza, I., Alharbi, M., Kling, M.F., Azzeer, A.M., 2019. Phase-matching mechanism for high-harmonic generation in the overdriven regime driven by few-cycle laser pulses. *arXiv1912.07918*.
- Schoun, S.B., Chirla, R., Wheeler, J., Roedig, C., Agostini, P., DiMauro, L.F., Schafer, K.J., Gaarde, M.B., 2014. Attosecond pulse shaping around a cooper minimum. *Phys. Rev. Lett.* 112, 153001. <https://doi.org/10.1103/PhysRevLett.112.153001>.
- Schoun, S.B., Camper, A., Salières, P., Lucchese, R.R., Agostini, P., DiMauro, L.F., 2017. Precise access to the molecular-frame complex recombination dipole through high-harmonic spectroscopy. *Phys. Rev. Lett.* 118, 033201. <https://doi.org/10.1103/PhysRevLett.118.033201>.
- Schultze, M., Fieß, M., Karpowicz, N., Gagnon, J., Korbman, M., Hofstetter, M., Neppl, S., Cavalieri, A.L., Komninos, Y., Mercouris, T., Nicolaides, C.A., Pazourek, R.,

- Nagele, S., Feist, J., Burgdörfer, J., Azzeer, A.M., Ernstorfer, R., Kienberger, R., Kleineberg, U., Goulielmakis, E., Krausz, F., Yakovlev, V.S., 2010. Delay in photoemission. *Science* 328, 1658–1662. <https://doi.org/10.1126/science.1189401>.
- Schultze, M., Ramasesha, K., Pemmaraju, C.D., Sato, S.A., Whitmore, D., Gandman, A., Prell, J.S., Borja, L.J., Prendergast, D., Yabana, K., Neumark, D.M., Leone, S.R., 2014. Attosecond band-gap dynamics in silicon. *Science* 346, 1348–1352. <https://doi.org/10.1126/science.1260311>.
- Shafir, D., Mairesse, Y., Villeneuve, D.M., Corkum, P.B., Dudovich, N., 2009. Atomic wavefunctions probed through strong-field light-matter interaction. *Nat. Phys.* 5, 412–416. <https://doi.org/10.1038/nphys1251>.
- Shan, B., Chang, Z., 2001. Dramatic extension of the high-order harmonic cutoff by using a long-wavelength driving field. *Phys. Rev. A* 65, 011804. <https://doi.org/10.1103/PhysRevA.65.011804>.
- Shan, B., Cavalieri, A.L., Chang, Z., 2001. Tunable high harmonic generation. In: *Applications of High Field and Short Wavelength Sources IX*. OSA, Washington, D.C., TuE18. <https://doi.org/10.1364/HFSW.2001.TuE18>.
- Shan, B., Ghimire, S., Chang, Z., 2005. Generation of the attosecond extreme ultraviolet supercontinuum by a polarization gating. *J. Mod. Opt.* 52, 277–283. <https://doi.org/10.1080/09500340410001729573>.
- Shiner, A.D., Trallero-Herrero, C., Kajumba, N., Bandulet, H.-C., Comtois, D., Légaré, F., Giguère, M., Kieffer, J.-C., Corkum, P.B., Villeneuve, D.M., 2009. Wavelength scaling of high harmonic generation efficiency. *Phys. Rev. Lett.* 103, 073902. <https://doi.org/10.1103/PhysRevLett.103.073902>.
- Shiner, A.D., Schmidt, B.E., Trallero-Herrero, C., Wörner, H.J., Patchkovskii, S., Corkum, P.B., Kieffer, J.C., Légaré, F., Villeneuve, D.M., 2011. Probing collective multi-electron dynamics in xenon with high-harmonic spectroscopy. *Nat. Phys.* 7, 464–467. <https://doi.org/10.1038/nphys1940>.
- Shu, Y., Fales, B.S., Levine, B.G., 2015. Defect-induced conical intersections promote non-radiative recombination. *Nano Lett.* 15, 6247–6253. <https://doi.org/10.1021/acs.nanolett.5b02848>.
- Silva, F., Teichmann, S.M., Cousin, S.L., Hemmer, M., Biegert, J., 2015. Spatiotemporal isolation of attosecond soft X-ray pulses in the water window. *Nat. Commun.* 6, 6611. <https://doi.org/10.1038/ncomms7611>.
- Sinha, A., Lee, J., Li, S., Barbastathis, G., 2017. Lensless computational imaging through deep learning. *Optica* 4, 1117–1125. <https://doi.org/10.1364/OPTICA.4.001117>.
- Slobodchikov, E., Moulton, P.F., 2011. 1-GW-peak-power, Cr:ZnSe laser. In: *CLEO:2011—Laser Applications to Photonic Applications*. OSA, Washington, D.C., PDPA10. https://doi.org/10.1364/CLEO_SI.2011.PDPA10.
- Slobodchikov, E., Chieffo, L.R., Wall, K.F., 2016. High peak power ultrafast Cr:ZnSe oscillator and power amplifier. In: *Solid State Lasers XXV: Technology and Devices*. SPIE, p. 972603. <https://doi.org/10.1117/12.2212793>.
- Smirnova, O., Mouritzen, A.S., Patchkovskii, S., Ivanov, M.Y., 2007. Coulomb–laser coupling in laser-assisted photoionization and molecular tomography. *J. Phys. B Atomic Mol. Phys.* 40, F197–F206. <https://doi.org/10.1088/0953-4075/40/13/F01>.
- Smirnova, O., Mairesse, Y., Patchkovskii, S., Dudovich, N., Villeneuve, D., Corkum, P., Ivanov, M.Y., 2009. High harmonic interferometry of multi-electron dynamics in molecules. *Nature* 460, 972–977. <https://doi.org/10.1038/nature08253>.
- Sola, I.J., Mével, E., Elouga, L., Constant, E., Strelkov, V., Poletto, L., Villoresi, P., Benedetti, E., Caumes, J.P., Stagira, S., Vozzi, C., Sansone, G., Nisoli, M., 2006. Controlling attosecond electron dynamics by phase-stabilized polarization gating. *Nat. Phys.* 2, 319–322. <https://doi.org/10.1038/nphys281>.

- Sorokina, I.T., 2004. Cr²⁺-doped II–VI materials for lasers and nonlinear optics. *Opt. Mater. (Amst.)* 26, 395–412. <https://doi.org/10.1016/j.optmat.2003.12.025>.
- Spielmann, C., Burnett, N.H., Sartania, S., Koppitsch, R., Schnürer, M., Kan, C., Lenzner, M., Wobrauschek, P., Krausz, F., 1997. Generation of coherent X-rays in the water window using 5-femtosecond laser pulses. *Science* 278, 661–664. <https://doi.org/10.1126/science.278.5338.661>.
- Stein, G.J., Keathley, P.D., Krogen, P., Liang, H., Siqueira, J.P., Chang, C.-L., Lai, C.-J., Hong, K.-H., Laurent, G.M., Kärtner, F.X., 2016. Water-window soft X-ray high-harmonic generation up to the nitrogen K-edge driven by a kHz, 2.1 μm OPCPA source. *J. Phys. B At. Mol. Opt. Phys.* 49, 155601. <https://doi.org/10.1088/0953-4075/49/15/155601>.
- Strickland, D., Mourou, G., 1985. Compression of amplified chirped optical pulses. *Opt. Commun.* 55, 447–449. [https://doi.org/10.1016/0030-4018\(85\)90151-8](https://doi.org/10.1016/0030-4018(85)90151-8).
- Takahashi, E.J., Kanai, T., Ishikawa, K.L., Nabekawa, Y., Midorikawa, K., 2008. Coherent water window X ray by phase-matched high-order harmonic generation in neutral media. *Phys. Rev. Lett.* 101, 253901. <https://doi.org/10.1103/PhysRevLett.101.253901>.
- Takahashi, E.J., Lan, P., Mücke, O.D., Nabekawa, Y., Midorikawa, K., 2013. Attosecond nonlinear optics using gigawatt-scale isolated attosecond pulses. *Nat. Commun.* 4, 2691. <https://doi.org/10.1038/ncomms3691>.
- Takeuchi, Y., Kawanaka, J., Fujita, M., 2009. Nonlinear refractive index of a YAG crystal at low temperature. In: *CLEO/Europe—EQEC 2009—European Conference on Lasers and Electro-Optics and the European Quantum Electronics Conference*. IEEE, p. 1. <https://doi.org/10.1109/CLEOE-EQEC.2009.5192480>.
- Tate, J., Auguste, T., Muller, H.G., Salières, P., Agostini, P., DiMauro, L.F., 2007. Scaling of wave-packet dynamics in an intense midinfrared field. *Phys. Rev. Lett.* 98, 013901. <https://doi.org/10.1103/PhysRevLett.98.013901>.
- Teichmann, S.M., Silva, F., Cousin, S.L., Hemmer, M., Biegert, J., 2016. 0.5-keV Soft X-ray attosecond continua. *Nat. Commun.* 7, 11493. <https://doi.org/10.1038/ncomms11493>.
- Vallin, J.T., Slack, G.A., Roberts, S., Hughes, A.E., 1969. Near and far infrared absorption in Cr doped ZnSe. *Solid State Commun.* 7, 1211–1214. [https://doi.org/10.1016/0038-1098\(69\)90179-3](https://doi.org/10.1016/0038-1098(69)90179-3).
- Vasilyev, S., Peppers, J., Moskalev, I., Smolski, V., Mirov, M., Slobodchikov, E., Dergachev, A., Mirov, S., Gapontsev, V., 2019. 1.5-mJ Cr:ZnSe Chirped Pulse Amplifier Seeded by a Kerr-Lens Mode-Locked Cr:ZnS Oscillator. *The Optical Society., ATu4A.4*. <https://doi.org/10.1364/assl.2019.atu4a.4>.
- Vincenti, H., Quéré, F., 2012. Attosecond lighthouses: how to use spatiotemporally coupled light fields to generate isolated attosecond pulses. *Phys. Rev. Lett.* 108, 113904. <https://doi.org/10.1103/PhysRevLett.108.113904>.
- Wang, H., Chini, M., Khan, S.D., Chen, S., Gilbertson, S., Feng, X., Mashiko, H., Chang, Z., 2009. Practical issues of retrieving isolated attosecond pulses. *J. Phys. B Atomic Mol. Phys.* 42, 134007. <https://doi.org/10.1088/0953-4075/42/13/134007>.
- Wang, H., Chini, M., Chen, S., Zhang, C.-H., He, F., Cheng, Y., Wu, Y., Thumm, U., Chang, Z., 2010. Attosecond time-resolved autoionization of argon. *Phys. Rev. Lett.* 105, 143002. <https://doi.org/10.1103/PhysRevLett.105.143002>.
- Wang, X., Chini, M., Cheng, Y., Wu, Y., Tong, X.-M., Chang, Z., 2013. Subcycle laser control and quantum interferences in attosecond photoabsorption of neon. *Phys. Rev. A* 87, 063413. <https://doi.org/10.1103/PhysRevA.87.063413>.
- Werme, L.O., Bergmark, T., Siegbahn, K., 1973. The L 2,3 MM auger spectrum of argon. *Phys. Scr.* 8, 149–153. <https://doi.org/10.1088/0031-8949/8/4/004>.

- Wheeler, J.A., Borot, A., Monchocé, S., Vincenti, H., Ricci, A., Malvache, A., Lopez-Martens, R., Quéré, F., 2012. Attosecond lighthouses from plasma mirrors. *Nat. Photonics* 6, 829–833. <https://doi.org/10.1038/nphoton.2012.284>.
- White, J., Chang, Z., 2019. Attosecond streaking phase retrieval with neural network. *Opt. Express* 27, 4799. <https://doi.org/10.1364/oe.27.004799>.
- Wong, M.C.H., Le, A.-T., Alharbi, A.F., Boguslavskiy, A.E., Lucchese, R.R., Brichta, J.-P., Lin, C.D., Bhardwaj, V.R., 2013. High harmonic spectroscopy of the cooper minimum in molecules. *Phys. Rev. Lett.* 110, 033006. <https://doi.org/10.1103/PhysRevLett.110.033006>.
- Wörner, H.J., Bertrand, J.B., Kartashov, D.V., Corkum, P.B., Villeneuve, D.M., 2010. Following a chemical reaction using high-harmonic interferometry. *Nature* 466, 604–607. <https://doi.org/10.1038/nature09185>.
- Wörner, H.J., Arrell, C.A., Banerji, N., Cannizzo, A., Chergui, M., Das, A.K., Hamm, P., Keller, U., Kraus, P.M., Liberatore, E., Lopez-Tarifa, P., Lucchini, M., Meuwly, M., Milne, C., Moser, J.-E., Rothlisberger, U., Smolentsev, G., Teuscher, J., van Bokhoven, J.A., Wenger, O., 2017. Charge migration and charge transfer in molecular systems. *Struct. Dyn.* 4, 061508. <https://doi.org/10.1063/1.4996505>.
- Wu, M., Chen, S., Camp, S., Schafer, K.J., Gaarde, M.B., 2016. Theory of strong-field attosecond transient absorption. *J. Phys. B Atomic Mol. Phys.* 49, 062003. <https://doi.org/10.1088/0953-4075/49/6/062003>.
- Wu, Y., Zhou, F., Larsen, E.W., Zhuang, F., Yin, Y., Chang, Z., 2019. Generation of 3 mJ, 44 fs, 2.5 micrometer pulses from a single-stage Cr²⁺:ZnSe amplifier. *arXiv* 1910.06650.
- Xiong, H., Xu, H., Fu, Y., Yao, J., Zeng, B., Chu, W., Cheng, Y., Xu, Z., Takahashi, E.J., Midorikawa, K., Liu, X., Chen, J., 2009. Generation of a coherent x ray in the water window region at 1 kHz repetition rate using a mid-infrared pump source. *Opt. Lett.* 34, 1747. <https://doi.org/10.1364/ol.34.001747>.
- Yarkony, D.R., 1996. Diabolical conical intersections. *Rev. Mod. Phys.* 68, 985–1013. <https://doi.org/10.1103/RevModPhys.68.985>.
- Yin, Y., Li, J., Ren, X., Zhao, K., Wu, Y., Cunningham, E., Chang, Z., 2016. High-efficiency optical parametric chirped-pulse amplifier in BiB₃O₆ for generation of 3 mJ, two-cycle, carrier-envelope-phase-stable pulses at 17 μ m. *Opt. Lett.* 41, 1142. <https://doi.org/10.1364/OL.41.001142>.
- Yin, Y., Ren, X., Chew, A., Li, J., Wang, Y., Zhuang, F., Wu, Y., Chang, Z., 2017. Generation of octave-spanning mid-infrared pulses from cascaded second-order nonlinear processes in a single crystal. *Sci. Rep.* 7, 11097. <https://doi.org/10.1038/s41598-017-11652-9>.
- Young, L., Ueda, K., Gühr, M., Bucksbaum, P.H., Simon, M., Mukamel, S., Rohringer, N., Prince, K.C., Masciovecchio, C., Meyer, M., Rudenko, A., Rolles, D., Bostedt, C., Fuchs, M., Reis, D.A., Santra, R., Kapteyn, H., Murnane, M., Ibrahim, H., Légaré, F., Vrakking, M., Isinger, M., Kroon, D., Gisselbrecht, M., L’Huillier, A., Wörner, H.J., Leone, S.R., 2018. Roadmap of ultrafast X-ray atomic and molecular physics. *J. Phys. B Atomic Mol. Phys.* 51, 032003. <https://doi.org/10.1088/1361-6455/aa9735>.
- Yun, H., Lee, K.-M., Sung, J.H., Kim, K.T., Kim, H.T., Nam, C.H., 2015. Resolving multiple molecular orbitals using two-dimensional high-harmonic spectroscopy. *Phys. Rev. Lett.* 114, 153901. <https://doi.org/10.1103/PhysRevLett.114.153901>.
- Yun, H., Yun, S.J., Lee, G.H., Nam, C.H., 2017. High-harmonic spectroscopy of aligned molecules. *J. Phys. B Atomic Mol. Phys.* 50, 022001. <https://doi.org/10.1088/1361-6455/50/2/022001>.
- Zahavy, T., Dikopoltsev, A., Moss, D., Haham, G.I., Cohen, O., Mannor, S., Segev, M., 2018. Deep learning reconstruction of ultrashort pulses. *Optica* 5, 666. <https://doi.org/10.1364/OPTICA.5.000666>.

- Zhao, K., Zhang, Q., Chini, M., Wu, Y., Wang, X., Chang, Z., 2012. Tailoring a 67 attosecond pulse through advantageous phase-mismatch. *Opt. Lett.* 37, 3891. <https://doi.org/10.1364/ol.37.003891>.
- Zhao, J., Sun, Y., Zhu, Z., Antonio-Lopez, J.E., Correa, R.A., Pang, S., Schülzgen, A., 2018. Deep learning imaging through fully-flexible glass-air disordered fiber. *ACS Photonics* 5, 3930–3935. <https://doi.org/10.1021/acsp Photonics.8b00832>.
- Zhu, Z., Sun, Y., White, J., Chang, Z., Pang, S., 2019. Signal retrieval with measurement system knowledge using variational generative model. *arXiv Prepr. arXiv1909.04188*.
- Zhu, Z., Huang, H.-H., Pang, S., 2020. Photon allocation strategy in region-of-interest tomographic imaging. *IEEE Trans. Comput. Imaging* 6, 125–137. <https://doi.org/10.1109/TCI.2019.2922477>.